Materials & Design 217 (2022) 110618

Contents lists available at ScienceDirect

Materials & Design

journal homepage: www.elsevier.com/locate/matdes

Designing the microstructural constituents of an additively manufactured near β Ti alloy for an enhanced mechanical and corrosion response

Avinash Hariharan [a,*], Phil Goldberg [a], Tobias Gustmann [a], Emad Maawad [b], Stefan Pilz [a], Frederic Schell [c], Tim Kunze [c], Christoph Zwahr [c], Annett Gebert [a]

[a] Institute for Complex Materials, IFW Dresden, Helmholtzstr. 20, 01069 Dresden, Germany
[b] Institute of Materials Physics, Helmholtz-Zentrum Hereon, Max-Planck-Str. 1, 21502 Geesthacht, Germany
[c] Fraunhofer Institute for Material and Beam Technology IWS, Winterbergstr. 28, 01277 Dresden, Germany

GRAPHICAL ABSTRACT

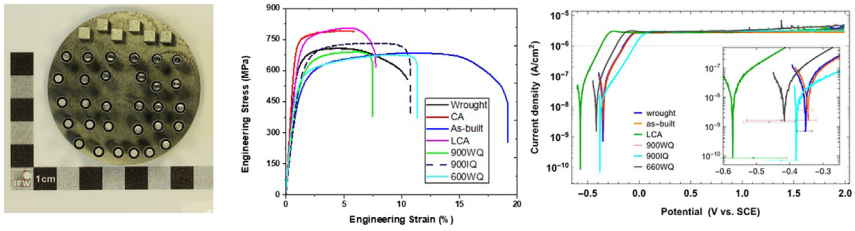

ARTICLE INFO

Article history:
Received 23 January 2022
Revised 11 March 2022
Accepted 1 April 2022
Available online 6 April 2022

Keywords:
Additive manufacturing (AM)
Laser powder bed fusion (LPBF)
Beta Titanium alloys
Corrosion

ABSTRACT

Additive manufacturing of near β-type Ti-13Nb-13Zr alloys using the laser powder bed fusion process (LPBF) opens up new avenues to tailor the microstructure and subsequent macro-scale properties that aids in developing new generation patient-specific, load-bearing orthopedic implants. In this work, we investigate a wide range of LPBF parameter space to optimize the volumetric energy density, surface characteristics and melt track widths to achieve a stable process and part density of greater than 99 %. Further, optimized sample states were achieved via thermal post-processing using standard capability aging, super-transus (900 °C) and sub-transus (660 °C) heat treatment strategies with varying quenching mediums (air, water and ice). The applied heat treatment strategies induce various fractions of α, martensite (α', α") in combination with the β phase and strongly correlated with the observed enhanced mechanical properties and a relatively low elastic modulus. In summary, our work highlights a practical strategy for optimizing the mechanical and corrosion properties of a LPBF produced near β-type Ti-13Nb-13Zr alloy via careful evaluation of processing and post-processing steps and the interrelation to the corresponding microstructures. Corrosion studies revealed excellent corrosion resistances of the heat-treated LPBF samples comparable to wrought Ti-13Nb-13Zr alloys.

1. Introduction

Metastable β-type Ti alloys are preferable new biomaterials with non-toxic compositions due to their ideal combination of excellent corrosion resistance, high strength and low elastic mod-

Abbreviations: AM, Additive Manufacturing; LPBF, Laser Powder Bed Fusion; SLM, Selective Laser Melting; UTS, Ultimate tensile strength; YS, Yield strength.

* Corresponding author.
E-mail address: a.hariharan@ifw-dresden.de (A. Hariharan).

https://doi.org/10.1016/j.matdes.2022.110618
0264-1275/

ulus (50 – 80 GPa) close to bone (~30 GPa) [1-6]. In β-Ti alloys, addition of Nb as an alloying element aids in stabilizing the β phase [7]. The ideal range for Nb concentration varies between 10 and 20 wt% or 35–45 wt% for fabricating β-Ti alloys with a low elastic modulus [5,7]. Deviation from this composition range increases the elastic modulus. Addition of Zr to the binary Ti-Nb alloys, in proportions of<20 wt%, is ideal for an enhanced solid solution strengthening of the β phase and allows for further exploitation of the martensitic phase fractions, to tune the microstructure, for enhancing the mechanical response and reducing the elastic modulus [8-10]. Various Ti-Nb-Zr alloy systems has been explored earlier [11-14]. However, the commercial Ti-13Nb-13Zr alloy, which is biocompatible and certified for surgical applications in accordance with the ASTM F1713 standards [15], is the focus of the present study. When subjected to capability aging (CA) heat treatment, the wrought alloy is expected to have a min. tensile strength of 860 MPa and a min. yield strength of 725 MPa coupled with a min. elongation of 8 % [15]. The mechanical properties of wrought Ti-13Nb-13Zr specimen are tailored using a combination of either forging, globularization, swaging, rolling, caliber rolling, arc-melting [16-18] and subsequent heat treatment. These approaches have helped to devise strategies to provide a range of mechanical properties including low elastic moduli of 50–80 GPa by tuning the microstructure with various phase fractions of martensite (α' (hexagonal), α'' (orthorhombic)) and β (cubic) phase [19–25]. Specifically, enhancing the volume fraction of the α'' phase (in one study at 51 % [20]) is found beneficial to lower the Young's modulus [27,28].

The alloying elements and process-controlled microstructures determine the corrosion behavior of Ti-13Nb-13Zr specimen in body fluids [29]. In electrochemical studies of differently heat-treated alloy specimens in Ringer's solution, water-quenched samples (with α' martensite) exhibited most stable oxide layers corresponding to lowest passive current densities compared to air-cooled and furnace-cooled samples. Their higher corrosion resistance was attributed to the uniform distribution of alloying elements in the phases and resulting low number of predominantly equiaxed β -grains. In a comparative wear and corrosion study [30] , Ti-6Al-4 V ELI alloys and Ti-13Nb-13Zr alloys, both water-quenched after heat treatment, showed similar corrosion resistance in Ringer's solution at 37 °C in the open-circuit condition. However, the Ti-6Al-4 V alloy exhibited a better anodic polarization performance than the Ti-13Nb-13Zr alloy despite the same martensitic microstructure (single α' phase). Furthermore, the furnace-cooled two-phase (α'+ β) Ti-6Al-4 V alloy possessed the lowest corrosion resistance due to the uneven distribution of alloying elements in various phases resulting in the unstable passive oxide film formation. In their more recent corrosion study on differently thermo-mechanically processed Ti alloys [31], the oxide film thickness and Nb_2O_5 content were found to be dependent of the thermomechanical state of the Ti-13Nb-13Zr alloy leading to the distinct formation ability and corrosion resistance of the oxide films on the cold rolled and hot rolled alloys. Hence, the formation and stability of passive oxide film were determined by the microstructural properties and the type of alloying elements as well as their distribution in the oxide film layer, further influencing the corrosion behavior of the Ti alloy surface.

However, recent advances in additive manufacturing (AM) have opened opportunities not only for near-net shape fabrication of complex specimen geometries, but also to tune the microstructure and thus, resulting mechanical and corrosion properties of such β-type Ti alloys [32-35]. This paves the way to the design of new patient-specific implants with an ideal combination of properties, which are better adapted to the *in vivo* conditions. The laser AM process (powder bed or powder fed) is capable of fabricating most metallic alloys, polymers and ceramics, and usually operates in an inert gas atmosphere, without the need of a high vacuum chamber unlike electron beam melting [36]. Laser powder bed fusion (LPBF), also known as selective laser melting (SLM), is one of the most important laser AM process, where a 3-dimensional component is fabricated by using a laser beam to melt successive layers of metal alloy powders. The laser melting process creates solidification cooling rates in the order of 10^4-10^6 K/s as a result of particularly smaller melt pools [37]. These exceptionally high cooling rates (compared to castings, water quenching and furnace cooling < 10^2 K/s [38]) can be leveraged to obtain various non-equilibrium microstructure states of Ti alloys. Microstructural entities such as grain size, precipitate size and volume fraction, crystallographic texture, grain boundary solute segregation can be tuned with suitable process parameters. Compared to the numerous LPBF studies on classical alloys, e.g. Ti-6Al-4 V these aspects are so far relatively unexplored for metastable, near β Ti alloys.

Earlier works on successfully fabricated AM β Ti alloys (for implant applications) with high part density include binary alloys Ti-X (Cr, Mo) [39,40], Ti-10Nb [41], Ti-42Nb [42], Ti-45Nb [43], Ti-27.5Nb [44] and Ti-50Ta [32] or multicomponent alloys such as TNZT and Ti2448 [45-48]. Most of these studies were focused on optimizing the mechanical properties and understanding the phase formation of the AM produced β Ti alloys with respect to the conventionally produced alloys. For example, Duan *et al.* [49] have shown that metastable β TMZF (Ti-12Mo-6Zr-2Fe) processed using LPBF had a high yield strength of 1 GPa, with a low modulus of 85 GPa coupled with a good ductility of 12 %. This was achieved by a coupled effect of α'' precipitation and controlling the growth texture during solidification.

In this regard, Ti-13Nb-13Zr alloys have been studied specifically in the wrought condition. Extensive studies on processing, microstructure and mechanical properties have been performed to enhance the strength and lower the elastic modulus. However, there are very limited studies on the effect of additive manufacturing and post processing treatments on the microstructure and mechanical properties of Ti-13Nb-13Zr. The first LPBF studies on Ti-13Nb-13Zr alloys [18,50,51] have shown that varying the scanning strategy and input energy density enhances the β volume fraction from 18 to 52 %. The LPBF fabricated samples are free of solidification cracks, that are typically observed in parts made from other metallic materials such as Al alloys or nickel based superalloys [37]. Importantly, these studies also reveal the complex microstructures of specimen made of this ternary alloy, consisting of nano-sized precipitates of α' martensite in the as-built samples, which can enhance the mechanical response of such alloys. Although the Young's modulus (from tensile tests along the building direction (BD)) of the as-built specimens were around 64 GPa, the presence of twins and preferentially oriented prior β grains in the microstructure along the building direction resulted in an enhanced mechanical response (tensile strength close to 1 GPa). However, a very low ductility of 2 % along BD was observed irrespective of the applied heat treatment strategies. Solution treatment with water quenching enhanced the yield strength by at least 10 %, however, the elastic modulus reduced by 15 % and in the range of 74–84 GPa [51]. Incidentally, the LPBF and subsequent heat treatment strategies have realized a poor ductility (2–5 %) of the Ti-13Nb-13Zr samples. Corrosion studies on LPBF-produced Ti-13Nb-13Zr alloys (in aerated Ringer's solution at room temperature) shows that the Nb and Zr oxides remains passive and aids in the corrosion resistance, compared to LPBF fabricated CP Ti and Ti-6Al-4 V [17]. However, the influence of the microstructural phase constituents, in the as-built and heat-treated variants of the LPBF-produced Ti-13Nb-13Zr alloy, on the corrosion resistance behavior has never been studied.

The current state of research regarding the fabrication of Ti-13Nb-13Zr specimen using LPBF reveals significant innovative

potential coupled with challenges. Alloy specimen in the as-built state exhibit better mechanical properties, i.e. lower elastic modulus (~64 GPa) than several other β-type Ti alloys. However, the heat treatment strategies used so far for LPBF-produced Ti-13Nb-13Zr specimen yielded a strengthening effect, only increased the elastic modulus by at least 15 % [17,51]. Achieving the standard high part density of up to 99 % poses another challenge for future work. The samples produced so far via LPBF only showed a maximum relative density of 98 %, further reduced the ductility of these alloys [18,51] and influenced the crack initiation under fatigue loading. Until today, the available data base of the microstructural, mechanical and corrosive response for LPBF-produced Ti-6Al-4 V [52,53], a classical implant alloy, far supersedes that of other metastable β Ti alloys, in particular Ti-13Nb-13Zr. Hence, the aim of our work is to enhance the understanding of the relationship between LPBF processing parameters, heat treatment conditions and the corresponding microstructures. The mechanical and corrosion performance of selected alloy states will be assessed and discussed in comparison to that of commercial wrought Ti-13Nb-13Zr and similarly heat-treated alloy specimens. This will enable the identification of optimal LPBF operation conditions in a fully laser-based processing chain for the fabrication of high performance Ti-13Nb-13Zr bone implants with best adapted biomechanical and surface biocompatible functionality [54].

In the current work, we perform a systematic exploration of the process parameter space (laser power and scan speed) for the LPBF of Ti-13Nb-13Zr alloy, to fabricate such near β-type alloys, to achieve a relative density of more than 99 %. The relationship between the input process parameter, especially the melt-track width, and the evolution of the microstructure during LPBF of such ternary near β -type alloys is analyzed. It was found that the microstructure of the LPBF samples fabricated with the optimized input energy parameter, is nearly martensitic (α' phase) with < 1 % β. Additionally, we explore super-transus and sub-transus heat treatment strategies to study the evolution of phase fraction during fast quenching and its influence on the tensile and corrosion properties. The synchrotron XRD is used to determine the phase fractions in the LPBF and heat-treated samples. Conventionally produced Ti-13Nb-13Zr alloys (from here on known by wrought) are also analyzed for the microstructure (wrought and heat-treated state) and tensile properties, to provide the necessary boundary condition to evaluate mechanical response of the LPBF-produced and heat-treated alloys. The corrosion studies reveal that all LPBF states exhibit an excellent corrosion resistance in phosphate-buffered saline solution, comparable to that of the as-received Ti-13Nb-13Zr samples without subsequent heat treatment.

2. Materials and methods

2.1. Alloy states and processing

Commercial wrought Ti-13Nb-13Zr rods (ASTM F1713 standard defined) of 50 mm diameter and 1500 mm length, were produced by Shaanxi Yunzhong Industry Development, China. The material was macroscopically homogeneous without any pores or cavities. A disc of 7 mm thickness and two bars of 5 mm × 5 mm × 100 mm were extracted by electrical discharge machining (EDM).

For the additive manufacturing process, gas atomized powders were produced from the wrought alloy rods via the EIGA (Electrode Induction melting inert gas atomization) (at Eckert TLS Technik GmbH, Germany). The powders (of size range between 20 and 60 μm) were characterized for their particle size distribution and particle morphology using the Camsizer X2 with X-Jet module (Microtrac Retsch GmbH). The X-Jet setup disperses particles through a nozzle which produces a constant particle flow, that is characterized using a high resolution ultrabright LED and digital cameras, that captures real time images at 300 frames per second. The images are post processed using the DIMENSIONS software. For statistical relevance, around 3 million powder particles were measured.

The chemical analysis of the commercial rod (wrought) material, the powders (three samples from different bottles of the same batch) as well as the LPBF parts was conducted using ICP-OES (inductively coupled plasma-optical emission spectroscopy, IRIS Intrepid II XUV from Thermo Fischer Scientific GmbH) regarding metal constituents. Carrier gas hot extraction (TC-436DR, LECO) was used for oxygen analysis.

All the LPBF samples were fabricated using a Realizer SLM 50 machine (DMG Mori) equipped with an infrared fiber lase source (1070 nm wavelength and maximum laser power of 125 W). The samples were built on a Ti-6Al-4V (grade 5) base plate and the base plate temperature was maintained at 50 °C. The entire process was performed under Ar atmosphere (O_2 content maintained below 1000 ppm). For LPBF process parameter optimization, cylindrical samples of 3 mm diameter and 6 mm height were fabricated. An additional and separated hollow a contour exposure (a thin hollow cylinder of rod 7 mm diameter, 11 m height fabricated concentrically to the main cylinder, with the same process parameter) was introduced for individual cylinders to investigate the influence of the line energy input on the final track/contour width [55,56]. The three important parameters that were employed in the SLM 50 Realizer, for the Ti-13Nb-13Zr alloy, are the point distance (10–60 μm), exposure time (20 – 120 μs) inside the scan vector, and the input laser power translates to 106 W – 125 W. Other LPBF parameters such as hatch distance (100 μm) the layer thickness (30 μm) were kept constant. To explore the process parameter window, the volumetric energy density (E_v in J/mm^3), estimated as P/(v*h*l), where, P: the input laser power (W), v: scanning speed (mm/s), h: hatching distance and l: layer thickness (μm), was strategically varied over 5 build jobs. The scanning vectors (stripe scanning) were rotated by 67° in adjacent layers. In total, 108 samples were fabricated (over 5 build jobs) and after removal from the base plate (using electrical discharge machining). All the samples were analyzed for their relative density (in %) by the Archimedean principle, using a Sartorius balance (MSA 225S). The relative densities were calculated using the theoretical density (5.005 g/cm^3) of Ti-13Nb-13Zr alloy with negligible solidification defects [57]. Additionally, all the samples were screened for surface quality.

Solution and ageing treatments for all samples were performed in a furnace (capsuled within a quartz tube under Ar atmosphere), to avoid surface oxidation. The samples after heat treatment were directly water or ice water quenched to room temperature. An overview of the different samples as well as the heat treatment strategies are summarized in Table 1. For identifying suitable heat treatment conditions, the β transformation temperature was determined using differential scanning calorimetry (DSC). Specimens with a weight of about 50 mg were measured at a heating/cooling rate of 10 °C/min in a Perkin-Elmer DSC 8500 between 27 and 950 °C. The specimens were cooled (- 10 °C/min) to room temperature using liquid nitrogen. Exemplary DSC heating and cooling curves for a LPBF-produced sample are shown in Supplementary 1. The exothermic peaks show that the α to β transformation during heating commences below 600 °C and peaks at 680 °C, finally ending at 770 °C. Hence, the β transition temperature is at 770 °C. The β transition temperature for LPBF-produced alloy states is ~ 40 °C higher than that for the wrought Ti-13Nb-13Zr state (reported in [4,20]) and nearly 90 °C more than reported values for LPBF-produced alloy [18]. Therefore, two super-transus and one sub-transus heat treatment strategies were designed, as schemat-

Table 1
Overview of the heat treatment strategies for the wrought and LPBF-produced Ti-13Nb-13Zr alloy samples.

Label	Sample preparation method
CA	Wrought alloy and heat-treated at 800 °C for 30 min with subsequent furnace-cooling, then heat-treated at 500 °C for 6 h with subsequent air-cooling (also known as capability aging (CA))
LCA	LPBF-specimens, heat-treated at 800 °C for 30 min with subsequent furnace-cooling, then heat-treated at 500 °C for 6 h with subsequent air-cooling
900WQ	LPBF-specimens, heat-treated at 900 °C for 1 h, then water-quenched (WQ)
900IQ	LPBF-specimens, heat-treated at 900 °C for 1 h, then ice-quenched (IQ)
660WQ	LPBF-specimens, heat-treated at 660 °C for 1 h, then water-quenched (WQ)

ically presented (Supplementary 1.). Additionally, the CA heat treatment (as prescribed by the ASTM F1713 standard [15]) was performed to wrought and LPBF alloys, as elucidated in Table 1.

2.2. LPBF part, microstructural and mechanical characterization

Optical micrographs of all LPBF samples were initially screened for the surface quality by using the digital confocal microscope Keyence VHX-6000. For microstructural analysis of various specimens, Cross-sections from the as-fabricated parts were prepared and subjected to standard metallographic techniques. Selected samples were polished with colloidal silica solution and etched with Kroll reagent (2 ml HF, 5 ml HNO_3, and 50 ml distilled water) for 10 s. Scanning electron microscopy (SEM) of the samples was conducted using a Zeiss Gemini Leo 1530 system.

Selected samples were investigated using X-ray computed tomography (μ-CT, Phoenix Nanotom, General Electric) The μ-CT analysis was conducted at 130 kV and 100 μA using a voxel size of 3 μm to analyze the volume fraction and distribution of pores. 1000 projections (1000 ms scanning time) were used for 3D-reconstruction of the sample volume, along with a beam collimator and a copper filter of 0.3 mm thickness. The volume analysis was performed using VG-Studio max 2.2 (Volume Graphics).

For X-ray diffraction (XRD), samples with a thickness of 300 μm were cut from the cylinders and manually ground to a thickness of<100 μm. X-ray diffraction (XRD) for powder and sample was carried out on a STOE STADIP diffractometer (STOE & Cie GmbH) with Mo-Kα_1 radiation (λ = 0.07093187 Å) in transmission mode. 2θ scans were made in the range of 10° to 60° with a step size of 0.01°. X'Pert High-Score Plus software and an ICSD PDF-2 plus database (ICSD, The Inorganic Crystal Structure Database, FIZ Karlsruhe) was used for indexing and post processing of the XRD data.

Synchrotron XRD (SXRD) experiments were conducted at the High Energy Materials Science (HEMS) beamline P07B operated by the Helmholtz-Zentrum Hereon at PETRA III, DESY. The wavelength of the synchrotron X-ray was 0.14235 Å, corresponding to X-ray energy of 87.109 keV. An incident beam size of 0.7 × 0.7 m m^2 was used. A PerkinElmer XRD 1622 flat panel detector with 2048 × 2048 pixels and a pixel size of 200x 200 μm^2 was utilized for diffraction pattern acquisition. The sample to detector distance (1426 mm) was calibrated using LaB_6 powder standard. The calibration, background subtraction and azimuthal integration (over 360°) of the 2D patterns were performed with Fit2D [58]. The X'Pert HighScore Plus software was used to quantitatively analyze the Fit2D-prepared data by means of the Rietveld refinement.

Ultrasonic measurements for precise determination of the Young's modulus were carried out on of wrought, LPBF and heat-treated samples, on cylindrical slices, with a diameter of 12 mm and thickness of 1.0 mm. The samples were prepared co-planar by grinding down to grade P4000 SiC paper. An Olympus 5900 PR (Hamburg, Germany) sender-receiver unit combined with a transducer V22-BC-RM (for transversal measurements) and type 2012 (for the longitudinal wave velocity measurements) was used. For the LPBF samples, the longitudinal axis of the test specimen was parallel to the LPBF building direction (BD).

Vickers microhardness tests were performed on polished samples using an HMV Shimadzu Microhardness tester with a pyramidal diamond indenter and a load of HMV 0.1 for 10 s. A matrix of 10 indentations was programmed at specific coordinates of the sample surface. The regions for the hardness testing were carefully selected so that the indentations were at least 0.1 mm away from the pores and defects in the microstructure. Room-temperature tensile tests were performed with a constant crosshead velocity corresponding to an initial strain rate of 10^{-3} s^{-1} in an Instron 5869 equipment. The tensile specimens (directly fabricated by LPBF) had a gauge length of 12.0 mm, width of 2.0 mm and thickness of 1.5 mm. The samples were mechanically polished until P4000 SiC paper. The strain was directly monitored at the sample using a video extensometer AVE2. The LPBF tensile samples were prepared with the tensile axis parallel to the building direction (BD) and transverse direction (TD). The samples for the wrought alloys were prepared with the tensile axis (loading direction) parallel to the longitudinal direction.

2.3. Corrosion studies

LPBF-fabricated and additionally heat-treated Ti-13Nb-13Zr cylinders of 15 mm length and 5 mm diameter were used as working electrodes in electrochemical corrosion studies. After attaching the electrical contact, the cylinders were embedded in epoxy resin to offer only a base surface, representing a sample cross section perpendicular to the SLM building direction, as the free electrode area to be exposed to the electrolyte during the corrosion measurement. For comparison, the wrought Ti-13Nb-13Zr sample with the same geometry was employed as a reference material. These studies were also performed on the heat-treated samples.

A thermostat-controlled double-wall glass cell with three electrode arrangement was employed for electrochemical measurements. Phosphate-buffered saline (PBS) solution (140 mM NaCl, 10 mM phosphate buffer, 3 mM KCl, pH 7.4 (at 25°); Merck Millipore), was used as electrolyte and was kept at a constant temperature of 37 ± 1 °C. A saturated calomel electrode (SCE = 0.241 V vs. SHE) combined with a Luggin capillary and a large area semi-cylindrical platinum mesh served as a reference electrode and a counter electrode, respectively. The corrosion cell setup was connected to the Solartron SI 1287 Electrochemical Interface. All potential values are given in Volts versus reference electrode (V vs. SCE).

Before each corrosion measurement, the working electrode surface was ground with abrasive SiC 1200-grade and subsequently 2500-grade paper, treated in an ultrasonic bath of water for a few minutes after each grinding procedure and finally rinsed with ethanol as well as pure water and air-dried. The freshly prepared electrode samples were stored in air for 20 h prior to immersion in the PBS solution to naturally passivate the surface in a defined manner.

Open circuit potential (OCP) measurements were carried out for up to 2 h to evaluate the corrosion behavior of the Ti-13Nb-13Zr surface under free corrosion conditions in the simulated body solution. Immediately after that, a potentiodynamic polarization measurement was conducted starting from an initial potential of 50 mV below the final OCP potential and the working electrode potential was scanned in the positive direction up to 2 V vs. SCE at a scan rate of 0.5 mV/s. Results were plotted in terms of current density as a function of the applied potential.

At least five corrosion measurements were performed for each sample type for reproducible evaluation and the corresponding electrochemical properties were either extracted from the measurement data or estimated by extrapolations (e.g. Tafel extrapolation). Arithmetic mean values and standard deviations were determined from the measurement data.

3. Results and discussion

The present study aims to analyze the relationship between LPBF process parameters with the microstructure and resulting mechanical and corrosive response of additively manufactured Ti-13Nb-13Zr parts. Firstly, a process optimization was performed to evaluate the impact of parameter windows on the morphology and part density of the LPBF specimen. Further, the most suitable parameter was used to fabricate the samples, which were subjected to an in-depth microstructure, mechanical and corrosion performance analysis. The results were compared with those obtained for wrought and capability aged (CA) Ti-13Nb-13Zr alloy samples.

3.1. Influence of LPBF process parameters on part morphology and density

Table 2 shows the chemical composition according to ASTM standard of the powders, wrought and the LPBF-produced Ti-13Nb-13Zr alloy. The composition of the samples produced in LPBF was found to be in very good agreement with the nominal alloy composition at all processing stages and within the limits defined in ASTM F1713 [15] including the dissolved oxygen content.

The as-received Ti-13Nb-13Zr alloy powders were evaluated for their chemical composition, particle size distribution and particle morphology. Fig. 1 (a and b) show typical SEM images of the powder particles revealing a high sphericity and smooth surface with minor signs of 'satellites'. This suggests good flowability and homogenous layer of the raw powders, which can ensure a high apparent density of the powder bed during the LPBF process.

Fig. 1 (c) is the particle size distribution (PSD) plot of the powders. The PSD of the powders from the analysis are d_{10} = 25.0 μm, d_{50} = 43.8 μm, d_{90} = 61.0 μm respectively. The mean particle size from the analysis was found to be around 42 μm. The anisotropy mean value (defined as the width-to-length ratio of the atomized powder particles) was 0.90, which further confirms good sphericity of the powder particles. The XRD plots shown in Fig. 1 elucidate that the phase fraction of the powders is predominantly the α' phase, as reported previously [18].

Fig. 2 (a) shows an optical image of a series of cylindrical and cube samples of LPBF Ti-13Nb-13Zr. All the samples were fabricated without any macroscopic cracks or delamination defects. Fig. 2(b) is the plot of the relative density of the LPBF-produced Ti-13Nb-13Zr samples measured by means of the Archimedean principle and plotted as a function of the volumetric energy density (E_v).

The plot clearly shows that the relative density of the samples varied from 92.5 % to 99.7 % (±0.2 %), as the input energy density was varied from 50 to 380 J/mm^3. To further investigate the defect density in the microstructure, three samples with decreasing relative densities were chosen. Fig. 2 (c-e) show the SEM micrographs of the cross sections of 3 selected samples along with the E_v, used for their fabrication. The sample (c) fabricated with a low energy input of ~ 12 J/mm^3 had the least part density of 93.5 %. The sample shows typical solidification defects from the LPBF process such as porosities and lack of fusion. The sample in Fig. 2 (d) showed the highest part density of 99.7 %, which is 1.5 % higher than reported for other LPBF-produced Ti-13Nb-13Zr alloys [18]. Most importantly, from this systematic process parameter analysis, a lower laser energy density input (25 – 50 J/mm^3) during the LPBF process resulted in at least 5 % of the Ti-13Nb-13Zr samples with part densities greater than 99 %.

Fig. 3 (a-b) are plots which show the variation of the track width and the corresponding average relative densities of the bulk sample, as a function of laser scanning speed and input laser powers (106 W, 116 W and 125 W respectively). The track widths were analyzed at four regions (that are diametrically opposite) as shown in the schematic inset. Fig. 3 (a) shows that for samples fabricated with laser scanning speed of 800 to 2000 mm s^{-1}, the track widths were in the range of 200–250 μm and the sample density values were at least 99 %. The sample with the highest part density of 99 % has a track width of 245 μm (highlighted with green arrow). The variation of track width and average relative density, as a function of the laser scan speed, is nearly constant. Plot (b) is the influence of the laser power on the track widths of samples fabricated with a scanning speed of 1250 mm s^{-1} (the laser scan speed used for fabricating the highest part density (99.7 %)). As the laser power increases, the track width fluctuates by 16 %, from the mean value of 240 μm. However, the part density reduced from 99.7 % to around 98.0 %. Additionally, process parameters which could eventually affect the surface quality of the parts were also eliminated, although the achieved part density was higher than 98 % (see Supplementary 2: (a-f)). Hence, this detailed process parameter analysis can further aid in developing an optimized process window for complex implant shapes, porous and lattice structures.

To further evaluate the 3D volume densities, X-ray μ-CT scans of 6 cylindrical samples, with an avg. relative density ≥ 99 % (from Fig. 3 (a)) were exclusively performed. Fig. 4 (a-e) are the optical images of the top surface of all the cylinders and their outer hollow contour scan with the corresponding 3D reconstruction images of the CT analysis arranged in the ascending order of their void fraction. Sample (a) and (b) showed the best surface finish with the percentage of voids (from μ-CT) being < 0.05 %. The sample (f) fabricated with the lowest energy density, albeit having an acceptable void fraction, has a poor surface quality with incomplete melting of the powders, especially in the outer layers of the cylinder.

Table 2
Summary of the chemical analysis (ICP-OES, carrier gas hot extraction) of the gas atomized powders.

Chemistry (wt.%)	Ti	Nb	Zr	Oxygen	Other trace elements
Nominal composition ASTM F1713	Bal.	12.5–14.0	12.5–14.0	<0.15	Negligible
Wrought Ti-13Nb-13Zr (commercial grade)	Bal.	13.8 ± 0.04	13.11 ± 0.1	< 0.055	Negligible
Gas atomized raw powder	Bal.	13.8 ± 0.05	13.11 ± 0.3	< 0.06	Negligible
LPBF Ti-13Nb-13Zr	Bal.	13.78 ± 0.15	13.16 ± 0.09	0.12 ± 0.03	Negligible

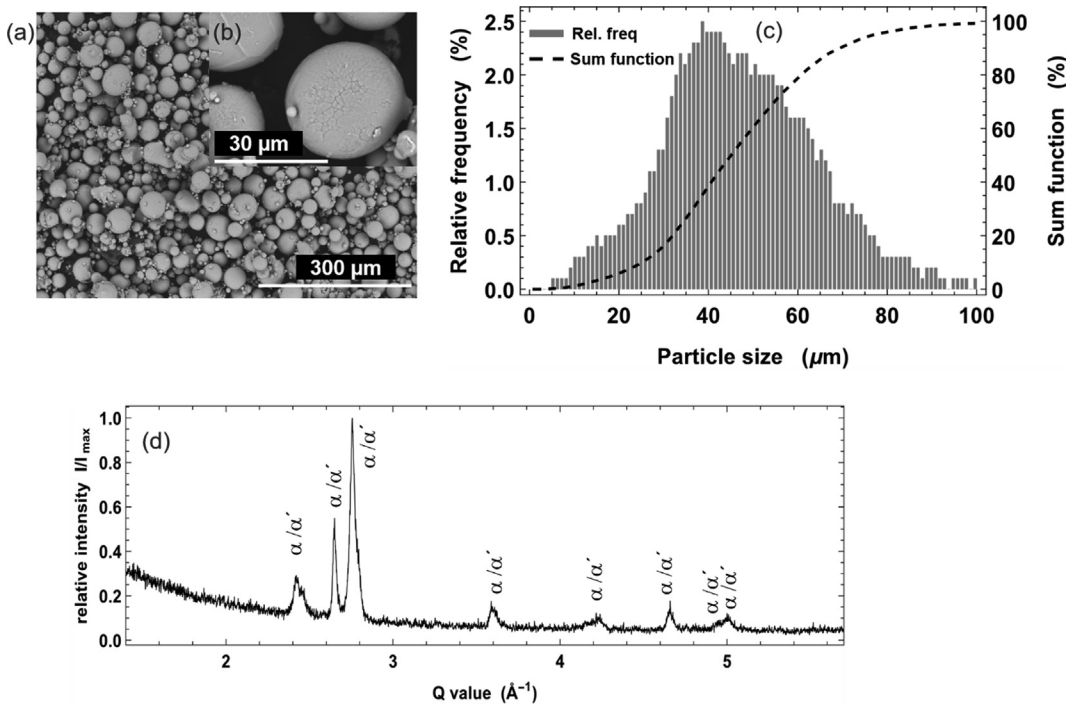

Fig. 1. SEM images of (a) the gas atomized powder particles of Ti-13Nb-13Zr (b) Satellites on powder particles. (c) Plot of the particle size distribution of the powder in as-received state. The particle size is characterized as the width of the powder. (d) The XRD pattern of gas atomized Ti-13Nb-13Zr powders.

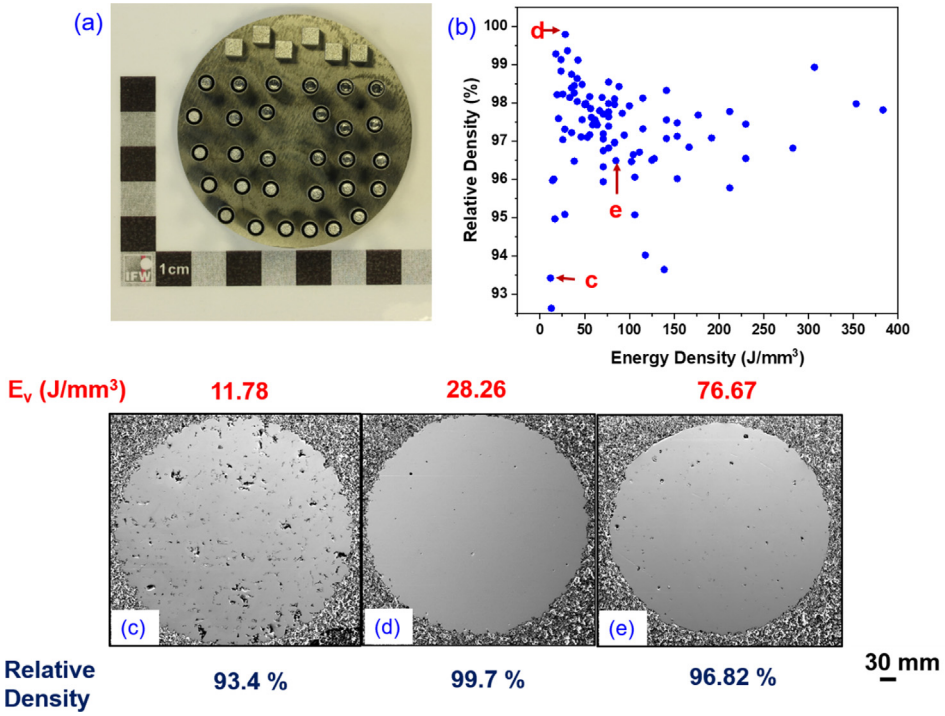

Fig. 2. (a) shows the cylindrical and cube specimens of Ti-13Nb-13Zr fabricated on a Ti base plate. (b) Plot showing variation of relative densities of all the samples fabricated with different Ev during LPBF. (c-e) SEM micrograph of selected specimens fabricated with Ev of<100 J / mm3. Sample (c) exhibits typical LPBF defects such as porosities and lack of fusion. Sample (d) has the highest density of 99.7 % with minimum solidification defects.

For all the subsequent studies in this work, the LPBF process parameter set of sample (a) was used. The process parameters and the corresponding sampled densities and track width values are summarized in Table 3. Subsequent LPBF build jobs (~40 samples) using the process parameter in Table 3, were analyzed for their relative density using the Archimedes principle. All the samples had an average density of ~ 99.7 %.

3.2. Microstructure analysis of LPBF and heat-treated samples vs. wrought

Fig. 5 summarizes SEM micrographs comparing the microstructures of Ti-13Nb-13Zr specimen in the wrought (a-b) and in the as-built LPBF condition (c-d). In the wrought condition (a), a two-phase microstructure of α needles in a matrix of β grains is

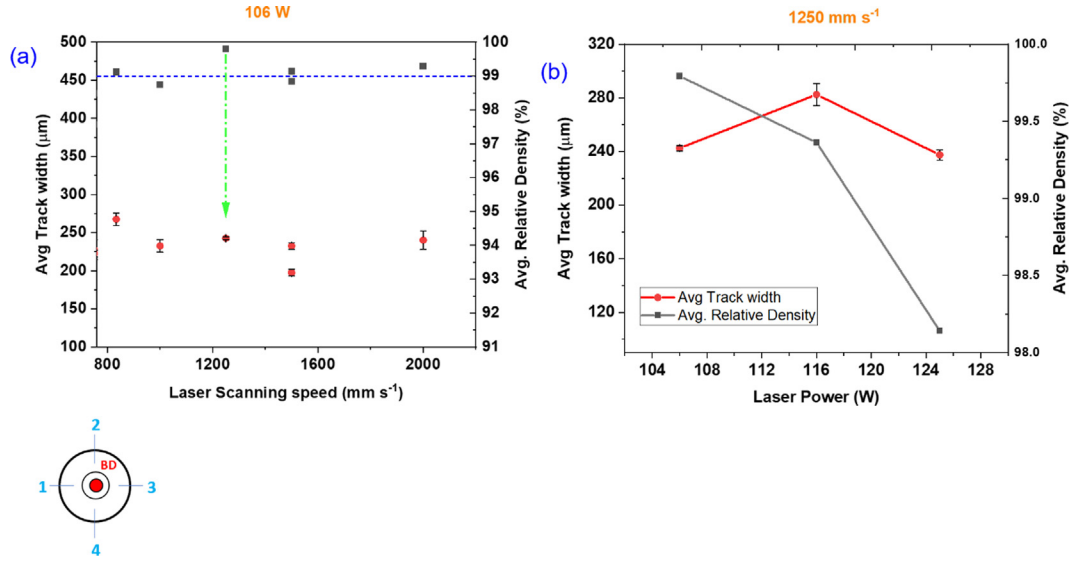

Fig. 3. Plot (a) shows the variation of track width (measured from the contour rings) and the corresponding average relative densities of the sample, as a function of laser scanning speed for samples fabricated with an input laser power of 106 W. Plot (b) is the influence of the 3 input laser power (106 W, 116 W and 125 W) on the track widths of samples fabricated at 1250 mm s^{-1}. The schematic inset illustrates the 4 measurement points on the contour rings for the track width analysis.

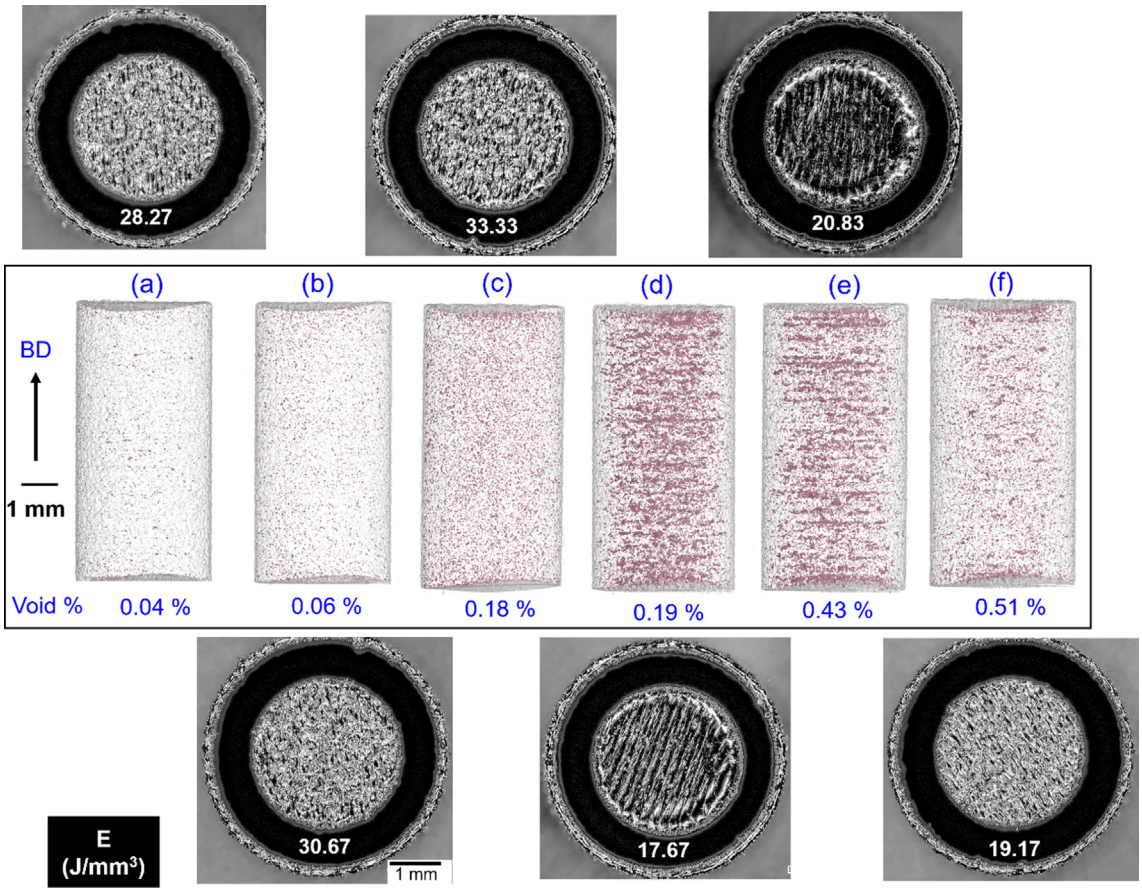

Fig. 4. (a-f) show the top view of the cylindrical sample and the corresponding outer scan and the corresponding 3D reconstruction images obtained via X-ray computed tomography (CT) for selected samples fabricated with the energy densities between 15 and 40 J/mm^3. The energy density values and the corresponding void % (from CT) are marked in red. (For interpretation of the references to colour in this figure legend, the reader is referred to the web version of this article.)

observed, corresponding to the slower cooling rate during the conventional process (10^1 – 10^2 K/s). Fig. 5 (d) shows a higher resolved SEM image, where fine α' phase laths (<100 nm) are detectable. LPBF processing is typically known to have faster cooling rates of the order 10^3 – 10^6 K/s [36,37,55]. As a result, fine scale laths, that are typical for the α' martensite [16,51] in such Ti alloys are observed in LPBF microstructures of Ti-13Nb-13Zr (Fig. 5 (c-d)). Coarse prior β grains (marked in Fig. 5 (c)), are oriented along

Table 3
Summary of the LPBF parameters for samples (a) that was selected after a comprehensive process parameter analysis.

Sample	Point distance (μm)	Exposure Time (μs)	Laser scanning speed (mm s^{-1})	Laser Power (W)	Vol. Energy Density (J/mm^3)	Avg. relative density from Archimedes method (%)	Void density from CT (%)	Track width (μm)
(a)	50	40	1250	106	28.27	99.70	0.04	242.5 ± 2.05

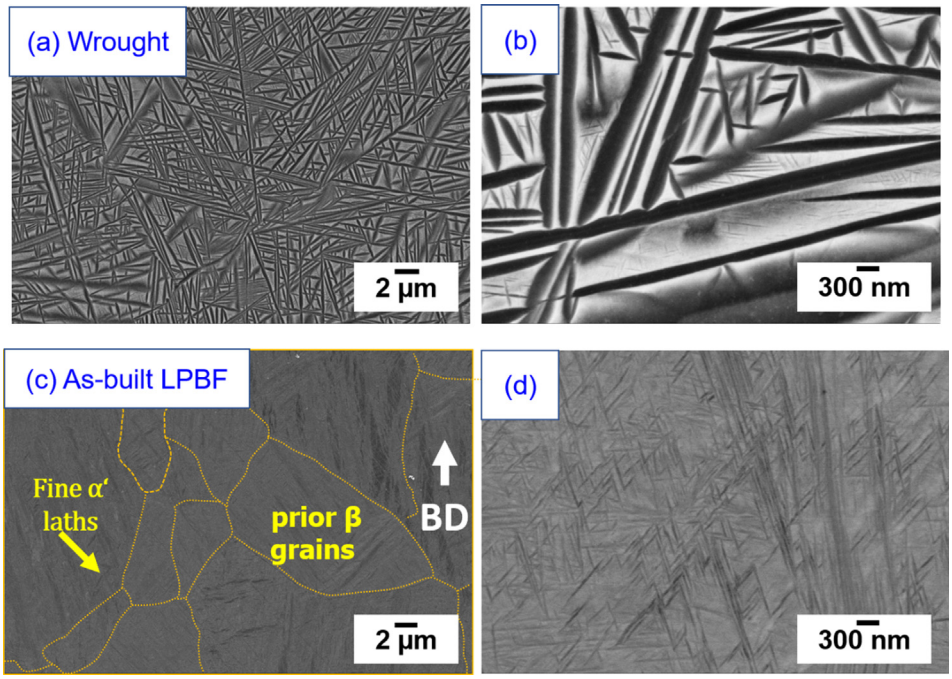

Fig. 5. SEM micrographs of (a-b) wrought and (c-d) as-built LPBF microstructures of Ti-13Nb-13Zr.

the build direction. The coarser grain structure (more than 30 μm, greater than the size of the layer thickness) and the overlapping prior β grains, typically seen in LPBF of Ti based β alloys, are due to the remelting phenomenon during the layer-by-layer solidification process [59].

Exemplary SEM-EDS maps in Fig. 6, shows the elemental distribution of Ti, Nb and Zr in an LPBF-produced samples, specifically along the build direction. No preferential solute segregation of Nb and Zr (due to the non-equilibrium solidification) in this length scale was observed. Similar observations have been reported in such LPBF-produced alloys [16]. The theoretical partitioning coefficients of Zr (0.86) and Nb (1.33) in Ti alloys obtained from the binary phase diagrams [60,61] clearly indicate that the β stabilizing Nb solute enriches the dendritic cores more than the interdendritic regions. Although the LPBF process is associated with the layer-by-layer heating cycles and subsequent phase transformations, a rather homogenous solute profile is observed at this length scale.

The XRD analysis, in Fig. 7, is focused on the wrought and CA samples. The XRD peaks exhibit primary α and β phases in both the wrought and CA samples respectively. To further evaluate the evolution of phases and the corresponding volume fraction, due to the various heat treatment procedures, synchrotron XRD measurements (SXRD) and analyses were performed (Fig. 8) for the as-built, and the heat-treated LPBF samples. The estimated volume fractions as well as the estimated lattice parameters of the associated phases (for all samples), weighted profile R-factor (R_{wp}) and the goodness of fit (χ^2) values are listed in Supplementary 3.

The SXRD peaks for an as-built sample correspond primarily to the α' phase and relatively small intensities of β peaks are observed (at 88°). The estimated volume fraction of the α' phase for the as-built samples are close to 99 % and with 1 % of β phase. This is a significantly high-volume fraction of α' martensite in comparison to values reported for other LPBF-produced Ti-13Nb-13Zr alloy specimen, [18,50]. The studies have shown that the microstructure constitutes of acicular α' martensite in a matrix of β. Additionally, the volume fraction of α' varied in the range of 18–52 %, and that for β between 48 and 82 % respectively, when the scanning rotation between individual layers were modified from 0°, 45° and 90° [50]. The evolution of these phases in Ti alloys is primarily dependent on the input laser energy density, which affects the time–temperature profile that a single layer experiences during solidification. Studies on LPBF-produced Ti alloys have shown that this "intrinsic heat treatment" (IHT) affects the formation and evolution of the α' martensitic structures within the prior β grains [53,62]. Therefore, it is highly plausible to get a nearly complete fine acicular α' martensitic microstructure in LPBF-produced Ti alloys, with a lean content of β stabilizers [53,62]. The "intrinsic" heating and cooling cycles are more pronounced in samples with higher energy inputs [62]. However, weaker "intrinsic" heating cycles, typically in low energy density input processing of β Ti alloys (<90 J mm^{-3}), almost exclusively exhibit such fine martensitic microstructures [53,62]. In the present study, the optimized energy density input for the as-built sample (28 J mm^{-3}) which falls well below the regime of a weaker IHT, leading to such a high-volume fraction of the α' martensitic microstructure, with less driving force for the transformation of the α' phase to β or β formed due to the decomposition of α' phase. The input laser energy density of 28 J mm^{-3} used to fabricate the current LPBF samples, is nearly 66 % lower than the input energy samples fabricated in previous works [18,50]. This decreased energy input leads to a weaker intrinsic heat treatment,

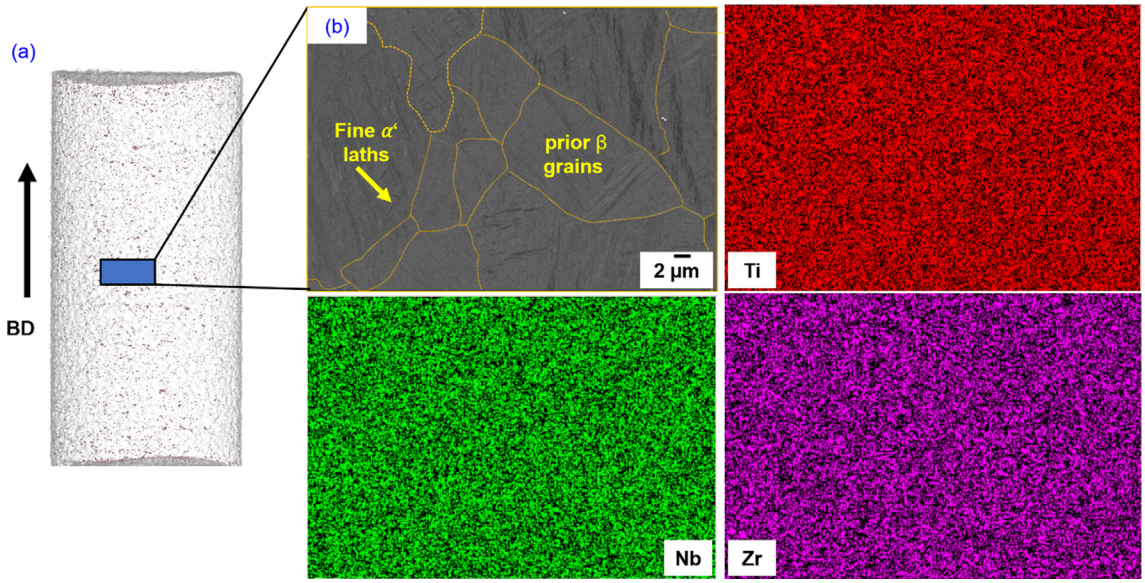

Fig. 6. (a) shows the CT image of the optimized sample, showing the region of interest for the EDS measurements (with respect to the building direction (BD)) and (b) are the SEM images and the corresponding EDS results showing the elemental distribution of Ti, Nb and Zr in LPBF-produced Ti-13Nb-13Zr sample.

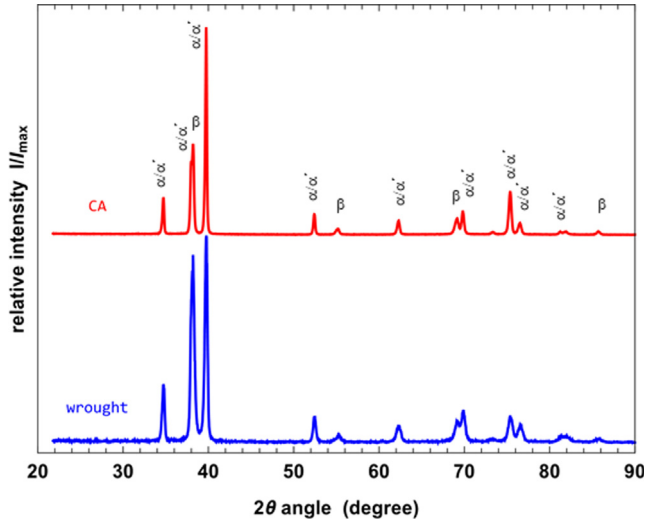

Fig. 7. XRD patterns of the wrought and CA samples of the Ti-13Nb-13Zr alloy.

hence leading to a complete martensitic microstructure with reduced β fraction.

The peaks for the LCA sample exhibit the familiar primary α and β phases, similar to both the wrought and CA samples respectively. The volume fractions of α (74 %) and β (26 %) phases in the LPBF LCA samples are similar to those in the wrought CA samples. Hence, the phase transformation from a complete martensitic microstructure in the LPBF fabricated samples, to an (α + β)-type (as a result of thermal equilibrium) occurs in similar lines to the wrought CA samples. The XRD peaks of samples subjected to the two super-transus heat treatment cycles namely 900WQ and 900IQ, exhibit the influence of the quenching rates on the microstructural evolution. Samples which were water quenched from 900 °C, exhibit a "composite" microstructure of the hexagonal α' (41.6 %), the orthorhombic α" (40 %) phases and a subsequent increase in the β fraction to 18.4 % relative to the as-built microstructure. Ice quenching potentially enhances the cooling rate relative to the room temperature water quenching process. The effect of this quenching mode is observed to enhance the fraction of the α" phase to ~ 46 %, with a slight reduction in the α' (41.6 %) and β (16.6 %) fractions.

Similar heat treatment strategies have been employed to wrought Ti-13Nb-13Zr, and the formation of the martensitic α' phase was observed in all the water quenched specimens, after the super-transus solution heat treatment [4,20]. Additionally, in Ti-Nb type alloys, the β → α" martensitic phase transformation can be observed when the alloy composition of Nb is between 13.1 wt% – 39.9 wt% coupled with a sufficiently fast cooling rate until room temperature (greater than the critical cooling rate) [63-65]. The martensite-starting temperature (M_s) for Ti-13Nb-13Zr is at 873 K and the martensite-finish temperature (M_f) is around 758 K [66]. For the Ti-Nb system, the Nb composition at which the M_s (α') equals that of the M_s (α") phase, occurs at 13.1 wt% [64,67]. Hence, it is plausible to obtain a mixed microstructure of the two martensitic phases in the quenched LPBF alloys post heat treatment. Since, the critical cooling rate of ice quenching is relatively higher than during water quenching (~1500 K/s [68]), it is a reasonable inference that this could have led to a difference in the fraction of α" of ~ 5 %. The increase in the volume fraction of the α" martensite for the ice quenched samples is consistent with the sub-zero quenching treatment reported for the wrought alloy [20]. The fraction of the β phase (presumably retained) varies by ~ 2 % between the 900IQ and 900WQ. Interestingly, in another study a super-transus treatment with water quenching of the LPBF-produced alloy showed ω phase precipitates [51]. However, the SXRD peaks (at 900WQ and 900IQ) in our work did not reveal any peaks for ω phase precipitates. Typically, such ω precipitates are formed in high β alloyed systems where a transition from α" to athermal ω occurs during quenching [69].

For the sub-transus heat treatment at 660 °C, the samples were water quenched from the α + β regime. The SXRD peaks reveal 3 phases, of the α', α" and β. The volume fraction of the β phase is nearly 2 times more than that in the 900WQ and 900IQ samples. However, the fraction of the α" phase reduced to 15 % and the microstructure has predominantly a high fraction of the α' phase (52.5 %) when compared to the 900WQ and 900IQ samples. Quenching of the samples from the α + β phase field region,

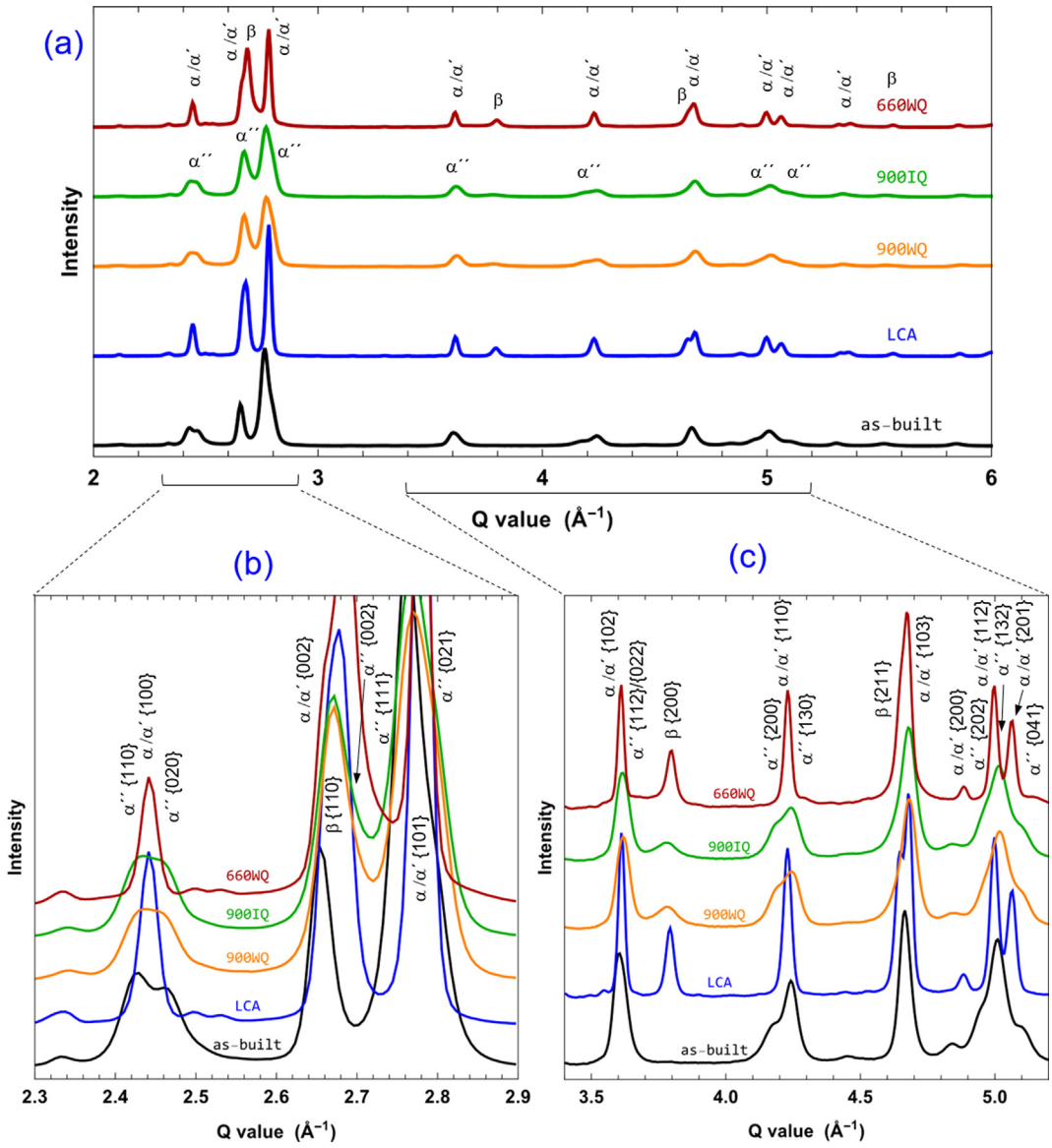

Fig. 8. SXRD patterns of the as-built and heat treated LPBF Ti-13Nb-13Zr samples. (a) The full intensity range of the XRD patterns, (b) and (c) are the magnified regions of the peaks for different samples and phases.

depending on the temperature, can result in a mixed microstructure [4,70], with a low volume fraction of the α'' phase [20].

Fig. 9 comprises a series of SEM images that show the effect of heat treatment strategies on the microstructure of wrought (along the longitudinal direction) and LPBF-produced Ti-13Nb-13Zr alloys (along BD). Fig. 9 (a1-a2) are the wrought and CA samples respectively. A typical lamellar microstructure of the dark α phase in a bright β matrix for titanium alloys is observed here. The grain size of the prior β grains was in the range of 200 – 1000 μm. The primary α laths are 100 nm in width. In addition, the secondary α laths are also visible, which are around 10 nm wide and 100 nm in length. In the CA samples, a similar lamellar type microstructure was observed. However, the widths of the α laths are 10 times larger than that in the wrought sample. It is a reasonable assumption that the as-received wrought alloy was processed with a higher cooling rate compared to the relatively slow cooling conditions during the CA heat treatment process.

Fig. 9 (b1-b4) are the SEM micrographs of the LPBF as-built and heat-treated specimens (LCA, 900WQ, 900IQ, 660WQ). As discussed previously (Fig. 5 (c)), the as-built microstructure is composed of nano-sized α' laths and precipitates. Figure (b2) is the microstructure of the LCA samples, exhibiting a similar α + β lamellar microstructure compared to that of the wrought CA samples Fig. 9 (a2).

Micrographs in b2 and b3 are the LPBF samples subjected to a super-transus heat treatment and water quenched to room temperature. They exhibit a martensitic microstructure, that is expected due to the higher cooling rate realized by water quenching, as compared to the relatively slower air cooling in the capability aging treatment, in a2 and b2 respectively [4]. The sub-transus (or the α + β regime) treatment of LPBF alloys (b5) also depicts a martensitic microstructure in a matrix of β grains.

3.3. Mechanical properties

Vickers microhardness testing was performed on the cross section of all the samples to understand the effect of LPBF process parameters on the microstructure and subsequent mechanical properties. The regions for the hardness testing were carefully chosen such that the indentations were at least 0.1 mm away from the

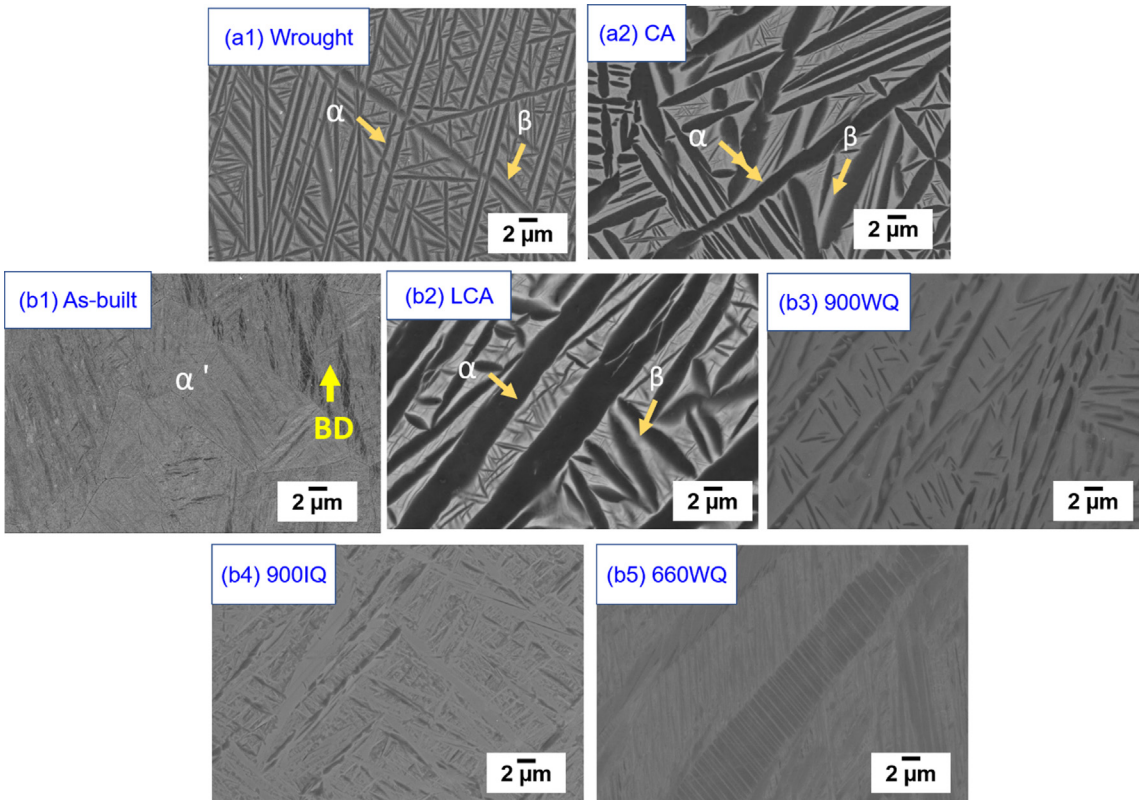

Fig. 9. Shows the SEM images of the effect of different heat treatment strategies on the microstructure of (a1) wrought, (a2) CA samples. The microstructures of the as built (b1) and the heat treated LPBF samples (b3-b4) are sequentially shown.

pores and defects in the microstructure. Fig. 10 (a) shows the variation of the Vickers hardness of all samples as a function of the input energy density. Interestingly, a strong scatter in the hardness values is observed and the range of the hardness varies from 240 Hv to 380 Hv. This scatter can be correlated to the inherent evolution of the residual stress within the microstructure, as a function of the input energy density coupled with the inherent phase transformations during the process that can alter the phase fractions at room temperature. Fig. 10 (b) is a summary plot that shows the effect of LPBF process parameters on the relative densities and Vickers microhardness of the Ti-13Nb-13Zr alloy, respectively. The critical region where the part density is more than 99 %, lies at energy density values between 20 and 50 J/mm^3 and a Vickers hardness value between 250 and 260 Hv. Although, samples at the top right of Fig. 10 (b) also show relative densities more than 99 %, due to the high input energy, the surface of these samples are oxidized. Hence, they were not considered.

With this comprehensive understanding of the microstructural phase fractions in the wrought, as-built LPBF samples, and their respective heat-treated counterparts (900WQ, 660WQ, and 900IQ), the mechanical responses of these microstructural states were evaluated. The mechanical properties for the wrought and LPBF alloys are evaluated along the build direction (BD) and longitudinal axis respectively.

Fig. 11 (a) are the plots that show the engineering stress–strain curves for all the samples subjected to uniaxial tension. Fig. 11 (b) shows the yielding behavior for the wrought, LPBF, and heat-treated samples in greater detail. As a result of the capability aging treatment, the CA alloys exhibit a higher yield strength and tensile strength compared to the wrought alloys. For the LPBF samples, the as-built samples (along BD) showed the highest elongation of ~ 17 % when compared to all the other LPBF heat treated samples. Thus, the ductility of the as-built sample state obtained in the present work is 70 % higher than those reported for LPBF Ti-13Nb-13Zr in other studies [16,18,71]. This significant improvement in the elongation values is due to the high sample density and reduced detrimental defects such as lack of fusion pores and local stress concentrators in the microstructure of the LPBF produced alloys. Zhou et al. reported that in their study for samples in the as-built state [16,18,71], the fraction of β phase is in the range of 18 – 52%, depending on the process parameters. Although the microstructure of the as-built sample exhibits a higher fraction of the β phase compared to our work, they attribute the reduction in ductility in the LPBF produced alloy to the lack of fusion pores and sharp defects at melt pool boundaries which acts as stress concentrators. Additionally, the presence of the grain boundary α' phase at interfaces of these β phase regions acts a nucleation point for fracture in Ti based alloys, hence reducing the ductility [16].

However, the yield strength and the ultimate tensile strength of the BD samples in the current work, is lower than the values reported [16,18,71]. This is attributed to the differences in the phase fractions observed in the microstructure, post-solidification. Although, the LPBF-processed alloys have a finer grain size [16], the enhanced mechanical response is once again attributed to the mixed microstructure of the grain boundary α' phases that decorate the β grains, which creates an enhanced resistance to deformation, specifically along the build direction, thereby increasing the yield strength [16]. However, in the current BD samples, the microstructure comprises a uniform α' martensitic phase, which is a softer phase when compared to a α' + β configuration. This could lead to a reduced tensile strength response in the BD samples. A similar yielding behavior of a completely α' martensitic Ti-13Nb-13Zr was observed relative to the other dual phase microstructures with β [19]. However, in the present work, the current optimized LPBF parameters, resulted in a part density of 99.70 %, which is higher compared to previous works. Hence, the

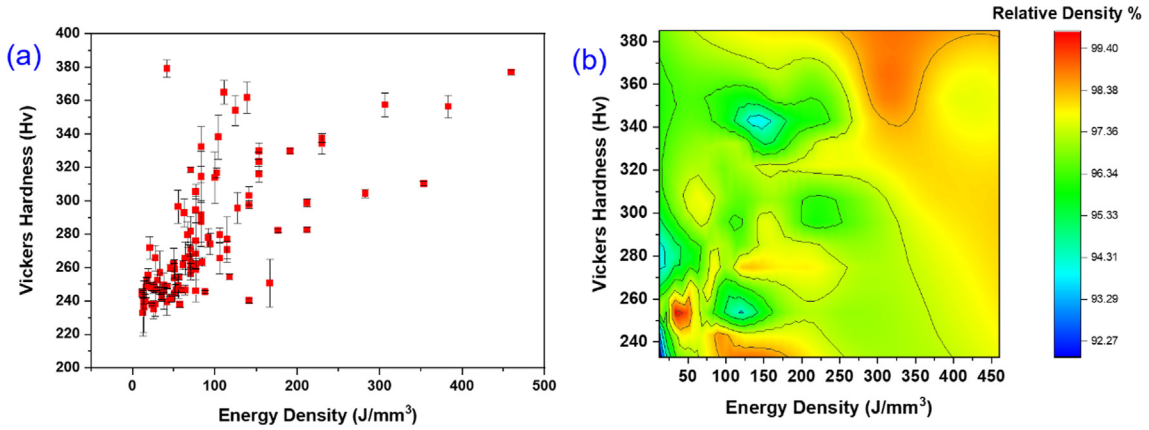

Fig. 10. Plots showing the (a) variation of Vickers Hardness as a function of input energy density, (b) 2D plot showing the variation of Vickers Hardness and relative densities measured for all samples, as a function of input energy density.

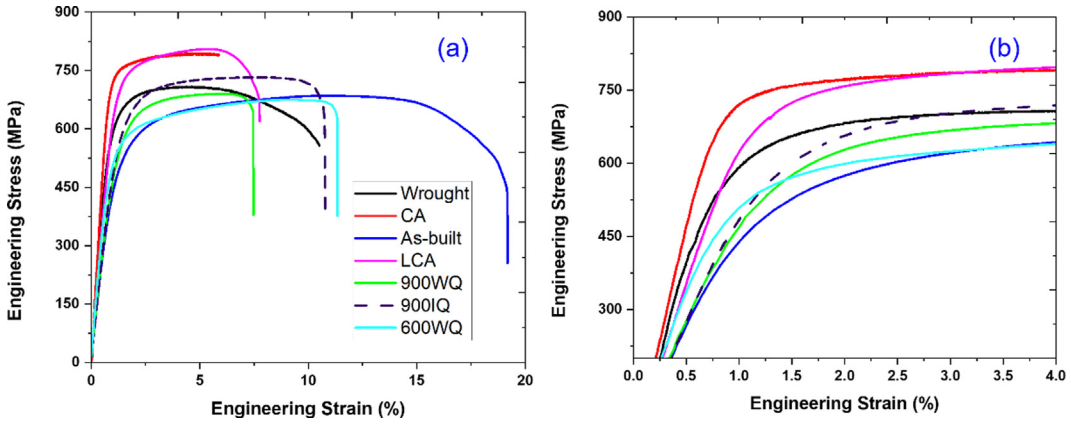

Fig. 11. The engineering stress strain curves for (a) samples subjected to tensile tests at an applied strain rate of 10^{-3} s^{-1} (b) shows the difference in the yielding behavior for the samples tested under tension.

microstructural state of the LPBF-produced samples is in an optimized condition.

Considering only the LPBF samples, the yield strength (YS) response can be categorized in the order, as-built < 900WQ < 660WQ < LCA < 900IQ. However, the tensile strength (UTS) of the samples follows a similar order, with an exception that 900IQ has a UTS value 8 % lower than LCA. With regard to the ductility, all the heat treatment strategies resulted in a total elongation to failure (%) in the range of 9–13 %.

Figure 12 (a-c) are the plots that show the influence of phase evolution due to the various heat treatment strategies on the mechanical properties of wrought and LPBF-produced alloys. The values are also summarized in Supplementary 4. Considering the wrought samples and CA samples, the fraction of α and β vary by 5 % after the CA heat treatment. As a result, the YS and the tensile strength of the CA samples increases by 10 % to the wrought samples. For the as-built sample, the fraction of α' is nearly 99 % with a small fraction of retained β. Hence, the tensile and yield strength are at least 10 % and 25 % less than the AR and CA samples. This can be attributed to the reduced β fraction and the formation of an elastically softer phase such as α'. With further CA heat treatment of the LPBF sample, the fraction of α + β phase increases, leading to an increase in the tensile and yield strength, at levels similar to the wrought and CA samples. However, the prior β grain size of the wrought and CA samples is in the range of 20 – 1000 μm, which is more heterogenous than the LCA samples. Therefore, the UTS and YS of LCA are at least 14 % higher. Similar variations in the values of the Vickers hardness for the wrought and CA samples were observed as a result of the changes on the phase fraction. However, the hardness of the as-built samples is higher than wrought and CA, as a result of evolution of residual stress in the microstructure, post solidification.

The higher Vickers hardness (greater than 500 Hv) reported in [18] for LPBF Ti-13Nb-13Zr is attributed to the high residual stresses and grain refinement. However, the higher β volume fraction in their work also contributes to the increased hardness. The Vickers hardness of the as-built samples in our study was evaluated at 257 Hv. The hardness of martensite is significantly lower than that of β in such Ti based alloys [72]. The acicular martensite in the as-built samples, is a supersaturated solid solution of α'. This contributes to the increase in the hardness. This mechanism of the hardness enhancement is also reported in previous studies in LPBF processed Ti alloys [62].

For the 900 WQ samples, the tensile strength, relative to the LCA decreases, as the phase fraction of the α' and α'' increases. Although, quenching from the solution temperature can enhance the solid solution strengthening, the presence of the softer α' and α'' martensite, of around 80 %, lowers the yield strength of the alloy [73]. For the 660WQ samples, a slight increase in the yield and tensile strength was observed. However, the 900IQ samples with the highest fraction of the α'' shows a further increase in the tensile and yield strength. Importantly, the yield strength of the LPBF heat-treated alloys is higher than that of the as-built sample. With further heat treatment the Vickers hardness in the fast quenched

alloys show a constant reduction, due to the enhanced formation of martensite phases, which have a lower hardness than the β phase [72]. Similar trends in the reduction in Vickers hardness were observed in the conventionally produced and heat treated Ti-13Nb-13Zr alloys [20].

Typically for martensitic microstructures the deformation proceeds under various mechanisms that are simultaneously activated [74,75]. The formation of martensite from the high temperature quenching process from the β phase involves differently oriented twins that are the variants of martensite [74,75]. In particular, the α" has 6 equivalent invariants [76,77]. Therefore, multiple and different deformation twinning modes are activated to accommodate the plastic deformation [76,77]. In general, the deformation mechanism in the β phase of Ti-Nb-Zr alloys is dependent on the stability of the β phase [78]. However, the macroscopic stresses are accommodated by either slip, twinning or strain induced martensitic transformation of β to α" [74]. These combined deformation mechanisms enhance the ductility of the Ti-Nb-Zr alloys. The shape memory effect and the super elasticity of these alloys is driven by the reversible stress induced martensitic transformation from β to α" [79]. For fully martensitic microstructures of Ti-Nb-Zr alloys, the deformation mechanism is governed by elastic deformation of the martensite, reorientation of the martensitic variants as a result of deformation twinning and plastic deformation due to dislocation motion under macroscopic tensile deformation [80-82]. The activation of the different twinning modes is strongly dependent on the lattice parameters of the β and α". In addition to the twinning modes of deformation, the deformation induced reverse martensitic transformation, i.e. from α"→ β, can also occur [78]. Therefore, such complex strain accommodation paths in the current microstructures, esp. in 900WQ, 660WQ and 900IQ samples, which contain varying amounts of α" phase need to be decoupled, in order to understand the enhancement of the yield strength from 900WQ to 900IQ. In-situ mechanical tests have been performed using the synchrotron XRD, to understand the microstructural texture and deformation behavior of the three water quenched specimens of LPBF Ti-13Nb-13Zr alloys. This will be a subject of another future study.

The elastic modulus of all the samples evaluated using ultrasonic testing and tensile testing have been summarized in Fig. 12 (c) as a function of the phase fraction evolution. The elastic modulus values obtained from both testing methods are consistent for all samples. Studies on the strong Nb compositional dependence of the elastic modulus and its subsequent effect on the phase fraction of α" and the β, in quenched binary β Ti-Nb alloys reveal that the variation in the modulus values is given by β < α" < α' < α < ω [27,28,32,83]. The as-built Ti-13Nb-13Zr alloy, consisting of a nearly complete martensitic microstructure, exhibits the lowest elastic modulus. Previous investigations have shown that the quenched martensite (α') in Ti-Nb alloys exhibit a low Young's modulus due to a maximum internal friction, inherent in the microstructure, due to the presence of defects such as twins and dislocations [84,85]. Additionally, the supersaturated (α') martensite exhibits an enhanced volume change which could further lower the elastic modulus [84,85].

Therefore, a combination of a microstructure with α" + β, which in the current scenario applies for the 900IQ samples, exhibits the lowest Young's modulus of 73 GPa, followed by the 900WQ samples with 78 GPa. As the α/α' phase increases in the 660WQ samples, an increase in the elastic modulus is observed. However, the CA and LCA samples that possess the highest fraction of the α phase exhibit the highest elastic modulus close to 93 GPa.

The mechanical properties of β Ti alloys, esp. Ti-13Nb-13Zr in the wrought state, are designed using a combination of process optimization techniques (PO) such as powder metallurgy, globularization, swaging, rolling, caliber rolling, arc-melting [16-18] or heat treatment optimization process (HPO) that includes super-transus or sub-transus temperatures with varying cooling rates [20], or using alloy design approaches that involves increasing or reducing the content of Nb and Zr, to fabricate other variants (OV) [86] of the Ti-Nb-Zr alloys. There approaches have helped devise strategies to provide a range of mechanical properties by tuning the microstructure. Recently, additive manufacturing of β-type Ti alloys have shown opportunities to design new compositions with biocompatible mechanical properties [32]. Fig. 13 (a-d) shows the UTS, YS and % elongation of PO, HTO, OV, and LPBF-produced Ti-13Nb-13Zr specimen. The mechanical properties of the wrought and LPBF Ti-13Nb-13Zr, and heat treated samples evaluated in this work are compared with all the above samples from literature [16,17,20,32,50,51,86,87]. The dashed line are the upper and lower bound of the mechanical properties reported for other compositions of additively manufactured β-type Ti alloys [32].

The UTS and YS values (a-b) obtained for the wrought, LPBF-produced and HT samples are comparable to most of the Ti-13Nb-13Zr and Ti-Nb-Zr alloy samples processed under various conditions. The present work clearly shows that the LPBF-produced Ti-13Nb-13Zr specimens, processed with a most suitable LPBF parameter set, requires further optimization, specifically to enhance the yield strength of the alloy. The capability ageing heat treatment of the wrought alloy samples and nearly martensitic LPBF alloy parts provided a similar enhancement in the mechanical properties. 3 different heat treatments were introduced to tune the microstructure with various phase fractions of martensite (α', α") and β phase. Hence, these heat treatment strategies to obtain a mixed microstructure, to trigger various deformation mechanisms, has resulted in an enhancement of the tensile and yield strength of the LPBF-HT alloys, in the range of other β-type Ti alloys, of wrought and LPBF fabricated alloys reported in literature. Additionally, the LPBF and HT variants have a pronounced ductility relative to most conventionally produced alloys (Fig. 13 (c)). Importantly, as-built alloys possess a lower elastic modulus compared to the heat-treated LPBF alloys (Fig. 13 (d)) and to other PO, HTO and OV alloys. Hence, the 900WQ and 900IQ heat treatment for LPBF-produced Ti-13Nb-13Zr provides a good strategy to enhance the tensile properties of the as-built alloy, while maintaining a good ductility and a lower Young's modulus of ~ 73 GPa.

3.4. Corrosion behavior

In earlier studies, the corrosion behavior of conventionally (cast and thermo-mechanically processed) fabricated Ti-13Nb-13Zr alloys states was analyzed and the effects of phases and grain morphologies on the electrochemical response was discussed [23,88].

Here, for the comparative evaluation of the corrosion properties of both sample types, i.e. LPBF-processed and wrought states, electrochemical studies were conducted in a simulated body fluid. Further, heat-treated samples were tested in order to assess the effect of heat-treatment related microstructure, as described in section 3.2, on the corrosion behavior.

Therefore, a Ti-13Nb-13Zr electrode sample (20 h air-aged) was immersed in a phosphate-buffered saline (PBS) solution at 37.5 °C, and firstly the open circuit potential (OCP) was monitored. The plots in Supplementary 5 shows exemplarily OCP transients for the Ti alloy sample types in the time range of 2 h. The shift of the OCP to positive values with time for both Ti alloy sample types, commercial and LPBF, indicates that the naturally air passivated surfaces were continuously further passivated. This behavior is very common for titanium-based materials and valve metals [89-96]. Depending on the specific surface state after sample preconditioning (e.g. grinding, air-aging and time after immersion (several seconds up to a few minutes)) the initial OCP values varied between the different samples. Specifically, heat-treated samples

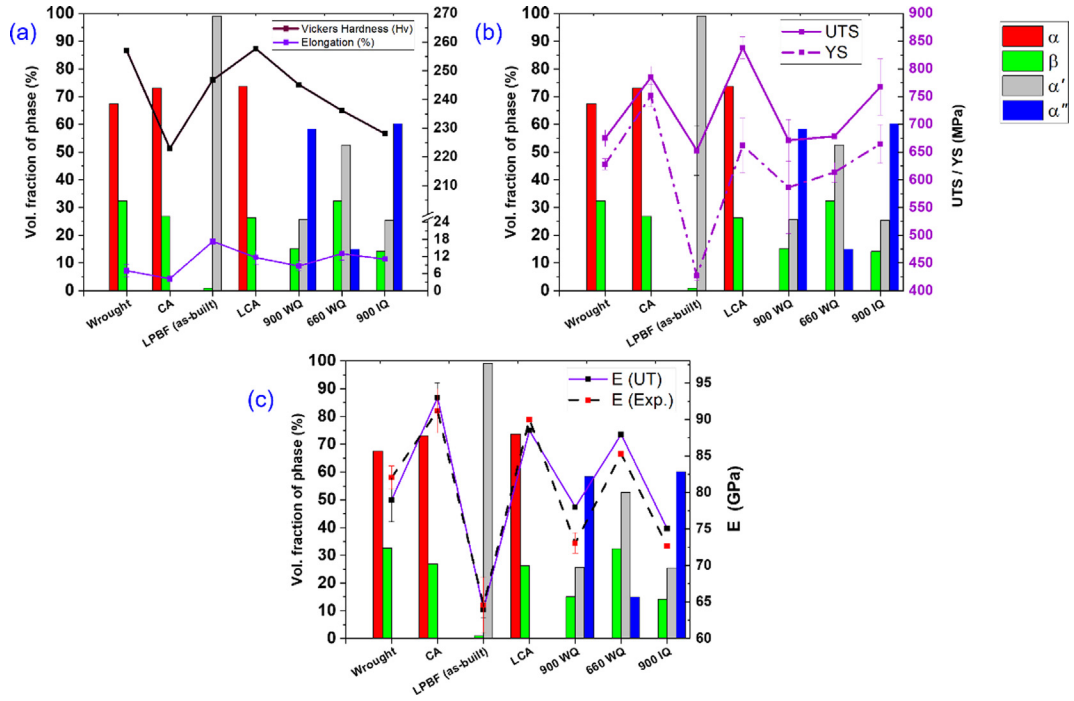

Fig. 12. (a-c) Plots showing the variation of the mechanical properties as function of the evolution of phases in the wrought, LPBF-produced and heat-treated samples of Ti-13Nb-13Zr.

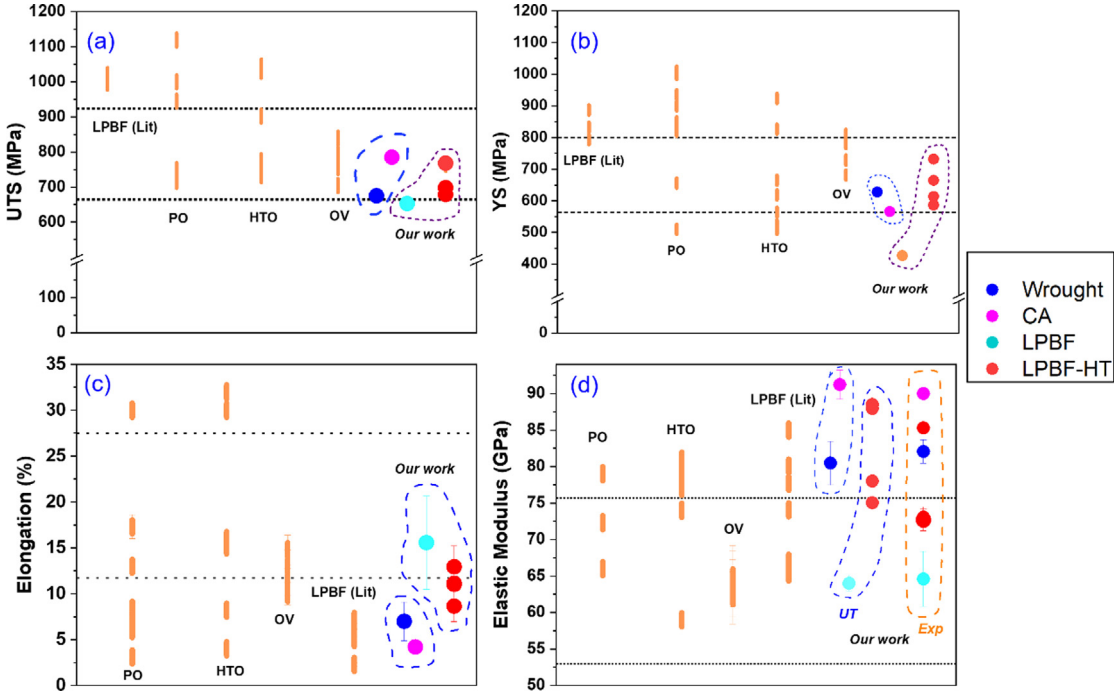

Fig. 13. (a-d) shows the UTS, YS and % elongation and elastic modulus properties of process optimized (PO), heat-treatment optimized (HTO) of conventionally produced Ti-13Nb-13Zr, other variants of Ti-Nb-Zr alloys (OV), LPBF-produced Ti-13Nb-13Zr. The mechanical properties of LPBF Ti-13Nb-13Zr and heat treated samples evaluated in this work are compared with all the above samples from literature [16,17,20,32,50,51,86,87]. The dashed line is the upper and lower bound of the properties from additively manufactured β Ti alloys (of different compositions) reported in [32]. For the elastic modulus of the alloys in this work (d), the values obtained from ultrasonic testing (UT) and tensile test (Exp) are highlighted.

showed a decrease in OCP within the first 30 min before the curve slope reversed and OCP shifted in the positive direction (Supplementary 5). This may be indicative of the instability of the native oxide layer at early stage of the OCP measurement, associated with the change of the oxidation state of the titanium oxide in the film and the formation of a mixed oxide layer [90]. The subsequent shift of the OCP potential towards positive values implies the oxide film recreation/restoration and thickening. The typical steady state end value, E_{OCP} , of slightly below −0.3 V vs. SCE after 2 h was obtained for the wrought and LPBF-processed samples (see Table 44). For

heat-treated samples this potential was in the range between −0.3 and −0.55 V vs. SCE.

Examples of subsequent potentiodynamic polarization measurements are shown in Fig. 14, revealing the typical behavior of Ti-based alloys with strong passivation ability. Mean values of corrosion parameters, as determined from at least 5 repeated polarization measurements for each sample type, are summarized in Table 4. The electrochemical value range obtained in this corrosion study is within the general range or in the order of magnitude of literature values for Ti-13Nb-13Zr alloy samples [29,97-99]. In the present study owing to all sample's history, i.e. long-term air aging and OCP immersion with related surface pre-passivation, the current density level in the vicinity of the corrosion potential E_{corr} was always extremely low indicating very low surface reactivity. Typical mean corrosion current density values range between i_{corr} = 86 ± 32nA/cm^2 for wrought states, i_{corr} = 51 ± 22nA/cm^2 for LPBF samples and lowest i_{corr} = 30 ± 29nA/cm^2 for additionally heat treated (900IQ) states. For all samples, the current density increased linearly with anodic potential scanning from the corrosion potential, and then remained nearly unchanged, indicative for the passive plateau. The passive regime started at absolutely about 0.4 V above the corrosion potential E_{corr} and the passive current densities measured at 0.5 V vs. SCE potential were slightly below 3 μA/cm^2 which indicates a high corrosion stability. Further, only insignificant increases in the anodic current density level were detected near and above 1.2 V vs. SCE potential, which may be attributed to the oxygen evolution reactions. Such a behavior is indicative of the strong barrier-type nature of the growing passive film on the valve metal-based alloy [29].

Regarding the influence of the specific microstructural state of the differently processed Ti-13Nb-13Zr alloys, the corrosion potential E_{corr} appears to be the most relevant parameter. Fig. 15 highlights the relationship between the phase composition of wrought, LPBF built and additionally heat-treated samples as summarized in Table 4, and the corrosion potentials derived from polarization measurements shown in Fig. 14.

Noteworthy, is that the E_{corr} values of the wrought and LPBF-processed samples have the smallest variation around the averaged potential value from at least 5 measurements per sample type. This implies an appearance of locally, more uniform electrode surface textures and therefore, a more homogeneous microstructure of the bulk sample. In contrast, as seen by the length of the error bars in the inset of Fig. 14 and in Fig. 15, the relatively larger deviation around the averaged E_{corr} of the heat-treated samples indicates locally, rather non-uniform surface textures with possibly some irregularities on the microscale. Despite significantly different microstructural states, the fine-grained as-built LPBF state (Figs. 6 and 10) mainly comprising α/α' phase fractions and the coarser grained α + β phase containing wrought state, reveal similar corrosion potential values in the range of about −0.350 V vs. SCE.

Additional heat treatment of LPBF samples leading to the LCA state yields the coarsest microstructure (Fig. 9) and a α + β phase composition which is similar to that of wrought states. The LCA state exhibits the most negative mean E_{corr} value, i.e. about 160 mV more negative than that of the wrought and LPBF states. This is typically indicative of a higher oxidation activity of the surface. However, other heat treatments of LPBF samples leads to negative but less pronounced shifts of the mean E_{corr} values, i.e. a shift of about 75 mV for samples annealed at 900 °C and of about ∼ 110 mV after 600 °C annealing. Besides an increase of the β phase fraction, the heat-treatments mainly trigger the formation of significant α" phase fractions and some structural coarsening (Fig. 9).

As shown in Fig. 9, the microstructures of different samples are distinct and thus the relative contents of α/α' and β phases. From the analysis of the temporal OCP evolution within 2 h (Supplementary 5) and by comparing the corrosion potential E_{corr} values of the different samples, the microstructural features, in particular the size distribution of the both α/α' and β phases on the surface, are considered as the most influential factor on the corrosion resistance. The sample in the LCA state showed the lowest corrosion potential out of all samples (Fig. 14 and Table 4) indicating the lowest corrosion resistance. The low corrosion resistance is correlated to the relatively high α phase content of the α + β microstructure, since a depletion of Nb and Zr oxides over the α/α' phase was found to decrease the stability of the oxide film in an electrolyte [100]. Furthermore, the difference in elemental composition between the two phases and thus the electrochemical activity, can cause the galvanic effect leading to an increased dissolution of the α/α' phase at the α/β phase boundary [101]. The ultrafine lamellar α/α' and β phases (as shown in Fig. 9) act as effective buffer layers to reduce the galvanic effect. Additionally, their ultrafine lamellar structures enable a pronounced formation of passive layers during the corrosion process due to their higher densities of

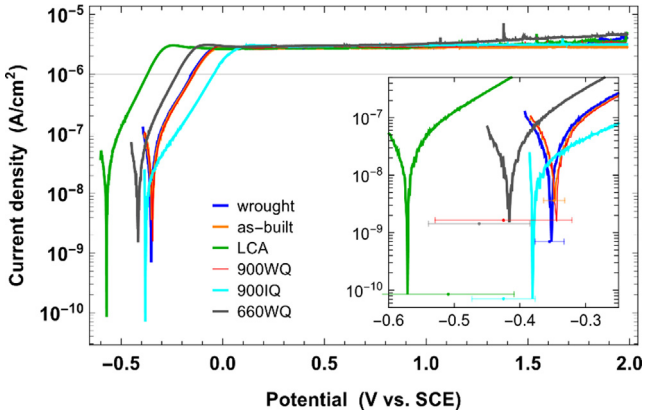

Fig. 14. Potentiodynamic polarization curves for as-cast and LPBF-processed Ti-13Nb-13Zr alloys in PBS solution at 37.5 °C. The inset shows the magnification in the potential range near the corrosion potential E_{corr}. Horizontal error bars indicate the standard deviation range around the averaged corrosion potential.

Table 4
Arithmetic means and standard deviations of the measured electrochemical values of the as-cast and LPBF-processed Ti-13Nb-13Zr alloys in PBS solution at 37.5 °C.

Ti-13Nb-13Zr	E_{OCP} (V vs. SCE)	E_{corr} (V vs. SCE)	i_{corr} (nA/cm^2)	i_p (at 0.5 V) (μA/cm^2)
wrought	−0.347 ± 0.022	−0.355 ± 0.022	86 ± 32	2.93 ± 0.31
as-built	−0.334 ± 0.017	−0.348 ± 0.016	51 ± 22	2.81 ± 0.11
LCA	−0.486 ± 0.109	−0.509 ± 0.100	36 ± 14	2.88 ± 0.18
900WQ	−0.399 ± 0.104	−0.425 ± 0.104	37 ± 29	2.81 ± 0.09
900IQ	−0.391 ± 0.064	−0.425 ± 0.048	30 ± 29	2.89 ± 0.17
660WQ	−0.442 ± 0.073	−0.462 ± 0.077	46 ± 19	2.91 ± 0.12

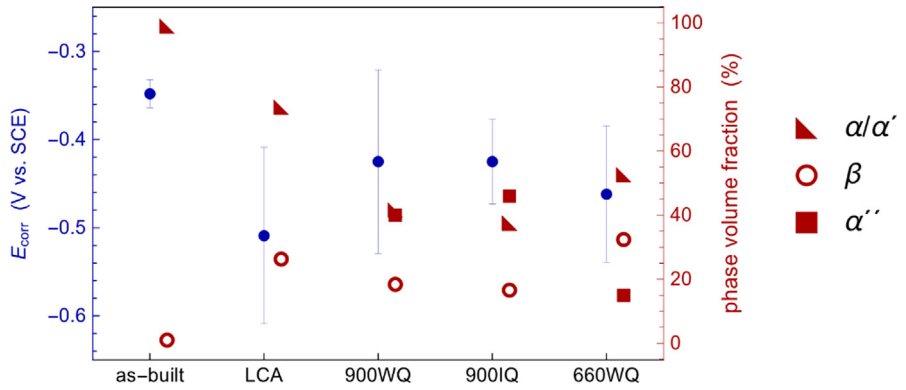

Fig. 15. Relationship between corrosion potential E_{corr} and volume fraction of the α/α', β andα" phase for the different LPBF Ti-13Nb-13Zr samples.

nucleation sites [102,103]. The low corrosion resistance is attributed to the uneven distribution of alloying elements in various phases resulting in the unstable passive oxide film formation [23,26]. Thus, the formation and stability of passive oxide film were determined by the microstructural properties and the type of alloying elements as well as their distribution in the oxide film layer, which further influences the corrosion behavior of the Ti alloy surface.

In summary, the as-built LPBF sample state exhibits the most positive corrosion potentials and thus, lowest surface reactivity out of all LPBF-processed samples. This is probably due to its most uniform microstructure consisting of very fine-grained α/α' phase fractions and (nearly) absence of the β phase. Additional heat-treatments of those samples not only induce coarsening effects, but lead also to more heterogeneous structural states with phase mixtures of α' and β phases as well as α" phase fractions. The resulting differently pronounced negative potential shifts may be related to a laterally less homogeneous oxide film growth with local differences in charge transfer rates and ion mobility [23].

However, when considering also corresponding corrosion current densities as well as anodic passive current densities (Fig. 15 and Supplementary 5), it can be stated that all LPBF states have an excellent corrosion resistance in PBS under the given conditions.

4. Conclusions

The near β-type Ti-13Nb-13Zr alloy is processed with the laser powder bed fusion (LPBF) additive manufacturing (AM) process and subjected to different heat treatment strategies. A detailed microstructure (in the as-built and heat-treated state) and mechanical properties analysis was performed. Additionally, the conventionally produced (wrought) Ti-13Nb-13Zr is treated and analyzed using the same techniques to provide the necessary boundary conditions to evaluate the LPBF-produced alloys. The synchrotron-based XRD technique was used to determine the phase fractions in the LPBF and heat-treated samples. Corrosion studies were conducted on wrought and LPBF samples to analyze their corrosion resistance.

Based on our studies, the following conclusions can be drawn:

1) The input laser power (<50 J mm^{-3}) and a subsequent lower melt track width of 240 μm aids in achieving part densities greater than 99 %. The low input energy parameter affects the as-built microstructure such that it forms a near fully martensitic α' state with < 1 % β.
2) The β transus of the LPBF samples was 770 °C, which is ~ 40 °C higher than that of the wrought alloy and nearly 90 °C more than reported values for same LPBF-produced alloy. The wrought and LPBF samples, when subjected to capability ageing heat treatment, reveal the classical 2 phase α + β microstructure. The super-transus (900 °C) and sub-transus (660 °C) heat treatment strategies reveal that the solution-treated LPBF samples have a mixed microstructure of β, α', α" due to the fast cooling (water (WQ) and ice (IQ) quenching). The highest volume fraction of the α" phase (46%) exists in the 900IQ specimens. The fraction of α" phase decreases from 900IQ > 900WQ (40 %) > 660WQ (15 %). The fraction of β reduces from 660WQ (32 %) >900WQ (18.4 %) > 900IQ (16.6 %).
3) The as-built LPBF alloys revealed a lower yield strength of 430 MPa, however had the maximum ductility of 17 %. For the solution treated and quenched samples, the presence of a three-phase microstructure, consisting of β, α', α", enhances the mechanical strength of the LPBF-produced alloys while retaining the level of ductility between 9 and 12 %. The yield strength varies as as-built < 900WQ < 660WQ < LCA < 900IQ. The presence of higher α" content in 900IQ and its subsequent deformation induced reverse martensitic transformation (i.e. from α"→β) could have enhanced its yield response. A combination of a microstructure with α" + β, which in the current scenario applies for the 900IQ samples, exhibits the lowest Young's modulus of 73 GPa, followed by the 900WQ samples with 78 GPa. Hence, the 900WQ and 900IQ heat treatment for LPBF-produced Ti-13Nb-13Zr provides a good strategy to enhance the tensile properties of the as-built alloy, while maintaining a good ductility and a lower Young's modulus.
4) The wrought and as-built LPBF samples showed the smallest deviations of the corrosion potential after at least 5 measurements, indicating the uniform distribution of the both phases and thus uniform oxide film growth during the spontaneous passivation. All heat-treated LPBF samples exhibited locally non-uniform microstructure containing different phases resulting in large variations of the corrosion potential. Despite their lower corrosion potentials compared to the wrought and as-built LPBF counterparts, all heat-treated LPBF samples showed passive current densities of about 3 μA/cm^2 similar to those of the wrought and as-built states which indicates an excellent corrosion resistance for all the investigated samples.

Declaration of Competing Interest

The authors declare that they have no known competing financial interests or personal relationships that could have appeared to influence the work reported in this paper.

Acknowledgements

This work was carried out in the framework of the OsteoLas project, partially financed by the European Regional Development Fund (EFRE) and by tax revenues on the basis of the budget adopted by the Members of the Parliament of Saxony (funding reference 100382988 / 100382989). S. Pilz acknowledges funding by the Deutsche Forschungsgemeinschaft (DFG) under project GE/1106/12-1 (no 419952351). We acknowledge DESY (Hamburg, Germany), a member of the Helmholtz Association HGF, for the provision of experimental facilities. Parts of this research were carried out at PETRA III P07 Beamline. We would like to thank Prof. Anand Kanjarla (IIT Madras, India) for the DESY synchrotron beam time.

Appendix A. Supplementary data

Supplementary data to this article can be found online at https://doi.org/10.1016/j.matdes.2022.110618.

References

[1] A. Reck, S. Pilz, M. Calin, A. Gebert, M. Zimmermann, Fatigue properties of a new generation ß-type Ti-Nb alloy for osteosynthesis with an industrial standard surface condition, Int. J. Fatigue. 103 (2017) 147–156, https://doi.org/10.1016/j.ijfatigue.2017.05.024.

[2] J. Vishnu, M. Calin, S. Pilz, A. Gebert, B. Kaczmarek, M. Michalska-Sionkowska, V. Hoffmann, G. Manivasagam, Superhydrophilic nanostructured surfaces of beta Ti[sbnd]29Nb alloy for cardiovascular stent applications, Surf. Coatings Technol. 396 (2020), https://doi.org/10.1016/j.surfcoat.2020.125965 125965.

[3] K. Zhuravleva, M. Bönisch, K. Prashanth, U. Hempel, A. Helth, T. Gemming, M. Calin, S. Scudino, L. Schultz, J. Eckert, A. Gebert, Production of Porous β-Type Ti–40Nb Alloy for Biomedical Applications: Comparison of Selective Laser Melting and Hot Pressing, Materials (Basel). 6 (2013) 5700–5712, https://doi.org/10.3390/ma6125700.

[4] M. Geetha, A.K. Singh, A.K. Gogia, R. Asokamani, Effect of thermomechanical processing on evolution of various phases in Ti–Nb–Zr alloys, J. Alloys Compd. 384 (2004) 131–144, https://doi.org/10.1016/J.JALLCOM.2004.04.113.

[5] M. Niinomi, Recent research and development in titanium alloys for biomedical applications and healthcare goods, Science and Technology of Advanced Materials 4 (5) (2003) 445–454.

[6] M. Niinomi, T. Hattori, S. Niwa, Material characteristics and biocompatibility of low rigidity titanium alloys for biomedical applications, Biomater. Orthop. (2003) 41–62, https://doi.org/10.1201/B14227-4/MATERIAL-CHARACTERISTICS-BIOCOMPATIBILITY-LOW-RIDIGITY-TITANIUM-ALLOYS-BIOMEDICAL-APPLICATIONS-MITSUO-NIINOMI-TOMOKAZU-HATTORI-SHIGEO-NIWA.

[7] D. Raabe, B. Sander, M. Friák, D. Ma, J. Neugebauer, Theory-guided bottom-up design of β-titanium alloys as biomaterials based on first principles calculations: Theory and experiments, Acta Mater. 55 (2007) 4475–4487, https://doi.org/10.1016/j.actamat.2007.04.024.

[8] K.M. Kim, H.Y. Kim, S. Miyazaki, Effect of Zr Content on Phase Stability, Deformation Behavior, and Young's Modulus in Ti–Nb–Zr Alloys, Mater. 13 (2020) 476, https://doi.org/10.3390/MA13020476.

[9] Y.L. Hao, S.J. Li, S.Y. Sun, R. Yang, Effect of Zr and Sn on Young's modulus and superelasticity of Ti–Nb-based alloys, Mater. Sci. Eng. A. 441 (2006) 112–118, https://doi.org/10.1016/J.MSEA.2006.09.051.

[10] M. Abdel-Hady, H. Fuwa, K. Hinoshita, H. Kimura, Y. Shinzato, M. Morinaga, Phase stability change with Zr content in β-type Ti–Nb alloys, Scr. Mater. 57 (2007) 1000–1003, https://doi.org/10.1016/J.SCRIPTAMAT.2007.08.003.

[11] R. Bolmaro, A.C. Parau, V. Pruna, M.A. Surmeneva, L.R. Constantin, M. Avalos, C.M. Cotrut, R. Tutuianu, M. Braic, D.V. Cojocaru, I. Dan, S. Croitoru, R.A. Surmenev, A. Vladescu, Investigation of cast and annealed Ti25Nb10Zr alloy as material for orthopedic devices, J. Mater. Res. Technol. 8 (2019) 3399–3414, https://doi.org/10.1016/J.JMRT.2019.06.006.

[12] M. Surmeneva, I. Grubova, N. Glukhova, D. Khrapov, A. Koptyug, A. Volkova, Y. Ivanov, C.M. Cotrut, A. Vladescu, A. Teresov, N. Koval, A. Tyurin, R. Surmenev, New Ti–35Nb–7Zr–5Ta Alloy Manufacturing by Electron Beam Melting for Medical Application Followed by High Current Pulsed Electron Beam Treatment, Met. 11 (2021) 1066, https://doi.org/10.3390/MET11071066.

[13] K.M. Kim, H.Y. Kim, S. Miyazaki, Effect of Zr Content on Phase Stability, Deformation Behavior, and Young's Modulus in Ti–Nb–Zr Alloys, Materials (Basel). 13 (2020) 476, https://doi.org/10.3390/ma13020476.

[14] Y.L. Hao, S.J. Li, S.Y. Sun, R. Yang, Effect of Zr and Sn on Young's modulus and superelasticity of Ti-Nb-based alloys, Mater. Sci. Eng. A. 441 (2006) 112–118, https://doi.org/10.1016/j.msea.2006.09.051.

[15] ASTM F1713 - 08(2013) Standard Specification for Wrought Titanium-13Niobium-13Zirconium Alloy for Surgical Implant Applications (UNS R58130), (n.d.). https://www.astm.org/Standards/F1713.htm (accessed March 9, 2021).

[16] L. Zhou, T. Yuan, R. Li, J. Tang, M. Wang, F. Mei, Anisotropic mechanical behavior of biomedical Ti-13Nb-13Zr alloy manufactured by selective laser melting, J. Alloys Compd. 762 (2018) 289–300, https://doi.org/10.1016/j.jallcom.2018.05.179.

[17] L. Zhou, T. Yuan, J. Tang, J. He, R. Li, Mechanical and corrosion behavior of titanium alloys additively manufactured by selective laser melting – A comparison between nearly β titanium, α titanium and α + β titanium, Opt. Laser Technol. 119 (2019) 105625.

[18] L. Zhou, T. Yuan, R. Li, J. Tang, G. Wang, K. Guo, J. Yuan, Densification, microstructure evolution and fatigue behavior of Ti-13Nb-13Zr alloy processed by selective laser melting, Powder Technol. 342 (2019) 11–23, https://doi.org/10.1016/j.powtec.2018.09.073.

[19] T. Lee, S. Lee, I.S. Kim, Y.H. Moon, H.S. Kim, C.H. Park, Breaking the limit of Young's modulus in low-cost Ti–Nb–Zr alloy for biomedical implant applications, J. Alloys Compd. 828 (2020), https://doi.org/10.1016/J.JALLCOM.2020.154401 154401.

[20] P. Kumar, G.S. Mahobia, V. Singh, K. Chattopadhyay, Lowering of elastic modulus in the near-beta Ti–13Nb–13Zr alloy through heat treatment, Mater. Sci. Technol. (United Kingdom) 36 (2020) 717–725, https://doi.org/10.1080/02670836.2020.1732608.

[21] T. Lee, K.T. Park, D.J. Lee, J. Jeong, S.H. Oh, H.S. Kim, C.H. Park, C.S. Lee, Microstructural evolution and strain-hardening behavior of multi-pass caliber-rolled Ti-13Nb-13Zr, Mater. Sci. Eng. A. 648 (2015) 359–366, https://doi.org/10.1016/j.msea.2015.09.062.

[22] C.A.R.P. Baptista, S.G. Schneider, E.B. Taddei, H.M. Da Silva, Fatigue behavior of arc melted Ti–13Nb–13Zr alloy, Int. J. Fatigue. 26 (2004) 967–973, https://doi.org/10.1016/J.IJFATIGUE.2004.01.011.

[23] M. Geetha, U. Kamachi Mudali, A.K. Gogia, R. Asokamani, B. Raj, Influence of microstructure and alloying elements on corrosion behavior of Ti–13Nb–13Zr alloy, Corros. Sci. 46 (2004) 877–892, https://doi.org/10.1016/S0010-938X(03)00186-0.

[24] C.H. Park, J.-W. Park, J.-T. Yeom, Y.S. Chun, C.S. Lee, Enhanced mechanical compatibility of submicrocrystalline Ti–13Nb–13Zr alloy, Mater. Sci. Eng. A. 527 (2010) 4914–4919, https://doi.org/10.1016/j.msea.2010.04.057.

[25] T. Lee, Y.U. Heo, C.S. Lee, Microstructure tailoring to enhance strength and ductility in Ti-13Nb-13Zr for biomedical applications, Scr. Mater. 69 (2013) 785–788, https://doi.org/10.1016/j.scriptamat.2013.08.028.

[26] I. Cvijović-Alagić, Z. Cvijović, S. Mitrović, V. Panić, M. Rakin, Wear and corrosion behaviour of Ti-13Nb-13Zr and Ti-6Al-4V alloys in simulated physiological solution, Corros. Sci. 53 (2011) 796–808, https://doi.org/10.1016/j.corsci.2010.11.014.

[27] S. Hanada, T. Ozaki, E. Takahashi, S. Watanabe, K. Yoshimi, T. Abumiya, Composition Dependence of Young's Modulus in Beta Titanium Binary Alloys, Mater. Sci. Forum. 426–432 (2003) 3103–3108, https://doi.org/10.4028/WWW.SCIENTIFIC.NET/MSF.426-432.3103.

[28] M. Niinomi, Mechanical biocompatibilities of titanium alloys for biomedical applications, J. Mech. Behav. Biomed. Mater. 1 (2008) 30–42, https://doi.org/10.1016/J.JMBBM.2007.07.001.

[29] M. Geetha, U. Kamachi Mudali, A.K. Gogia, R. Asokamani, B. Raj, Influence of microstructure and alloying elements on corrosion behavior of Ti-13Nb-13Zr alloy, Corros. Sci. 46 (2004) 877–892, https://doi.org/10.1016/S0010-938X(03)00186-0.

[30] I. Cvijović-Alagić, Z. Cvijović, S. Mitrović, V. Panić, M. Rakin, Wear and corrosion behaviour of Ti–13Nb–13Zr and Ti–6Al–4V alloys in simulated physiological solution, Corros. Sci. 53 (2011) 796–808, https://doi.org/10.1016/J.CORSCI.2010.11.014.

[31] I. Cvijović-Alagić, Z. Cvijović, J. Bajat, M. Rakin, Composition and processing effects on the electrochemical characteristics of biomedical titanium alloys, Corros. Sci. 83 (2014) 245–254, https://doi.org/10.1016/j.corsci.2014.02.017.

[32] S. Bahl, S. Suwas, K. Chatterjee, Comprehensive review on alloy design, processing, and performance of β Titanium alloys as biomedical materials, Int. Mater. Rev. 66 (2) (2021) 114–139.

[33] P.C. Collins, D.A. Brice, P. Samimi, I. Ghamarian, H.L. Fraser, Microstructural Control of Additively Manufactured Metallic Materials, Annu. Rev. Mater. Res. 46 (2016) 63–91, https://doi.org/10.1146/annurev-matsci-070115-031816.

[34] A. Kreitcberg, V. Brailovski, S. Prokoshkin, New biocompatible near-beta Ti-Zr-Nb alloy processed by laser powder bed fusion: Process optimization, J. Mater. Process. Technol. 252 (2018) 821–829, https://doi.org/10.1016/j.jmatprotec.2017.10.052.

[35] S.L. Sing, W.Y. Yeong, F.E. Wiria, Selective laser melting of titanium alloy with 50 wt% tantalum: Microstructure and mechanical properties, J. Alloys Compd. 660 (2016) 461–470, https://doi.org/10.1016/j.jallcom.2015.11.141.

[36] P. Bajaj, A. Hariharan, A. Kini, P. Kürnsteiner, D. Raabe, E.A. Jägle, Steels in additive manufacturing: A review of their microstructure and properties, Mater. Sci. Eng. A. 772 (2020), https://doi.org/10.1016/J.MSEA.2019.138633 138633.

[37] A. Hariharan, L. Lu, J. Risse, A. Kostka, B. Gault, E.A. Jägle, D. Raabe, Misorientation-dependent solute enrichment at interfaces and its contribution to defect formation mechanisms during laser additive manufacturing of superalloys, Phys. Rev. Mater. 3 (2019), https://doi.org/10.1103/PhysRevMaterials.3.123602 123602.

[38] J. Van Humbeeck, Microstructure and mechanical properties of Selective Laser Melted, 00 (2011).

[39] T. Nagase, T. Hori, M. Todai, S.H. Sun, T. Nakano, Additive manufacturing of dense components in beta-titanium alloys with crystallographic texture from a mixture of pure metallic element powders, Mater. Des. 173 (2019), https://doi.org/10.1016/J.MATDES.2019.107771 107771.
[40] M. Todai, T. Nagase, T. Hori, H. Motoki, S.H. Sun, K. Hagihara, T. Nakano, Fabrication of the beta-titanium alloy rods from a mixture of pure metallic element powders via selected laser melting, Mater. Sci. Forum. 941 (2018) 1260–1263, https://doi.org/10.4028/WWW.SCIENTIFIC.NET/MSF.941.1260.
[41] M.A. Surmeneva, A. Koptyug, D. Khrapov, Y.F. Ivanov, T. Mishurova, S. Evsevleev, O. Prymak, K. Loza, M. Epple, G. Bruno, R.A. Surmenev, In situ synthesis of a binary Ti–10at% Nb alloy by electron beam melting using a mixture of elemental niobium and titanium powders, J. Mater. Process. Technol. 282 (2020), https://doi.org/10.1016/J.JMATPROTEC.2020.116646 116646.
[42] C. Schulze, M. Weinmann, C. Schweigel, O. Keßler, R. Bader, Mechanical properties of a newly additive manufactured implant material based on Ti-42Nb, Materials (Basel). 11 (1) (2018) 124.
[43] H. Schwab, K.G. Prashanth, L. Löber, U. Kühn, J. Eckert, Selective Laser Melting of Ti-45Nb Alloy, Met. 5 (2015) 686–694, https://doi.org/10.3390/MET5020686.
[44] M. Fischer, P. Laheurte, P. Acquier, D. Joguet, L. Peltier, T. Petithory, K. Anselme, P. Mille, Synthesis and characterization of Ti-27.5Nb alloy made by CLAD® additive manufacturing process for biomedical applications, Mater. Sci. Eng. C. 75 (2017) 341–348, https://doi.org/10.1016/j.msec.2017.02.060.
[45] R.L. Batalha, W.C. Batalha, L. Deng, T. Gustmann, S. Pauly, C.S. Kiminami, P. Gargarella, Processing a biocompatible Ti-35Nb-7Zr-5Ta alloy by selective laser melting, J. Mater. Res. 35 (9) (2020) 1143–1153.
[46] C.H. Ng, M.J. Bermingham, M.S. Dargusch, Eliminating segregation defects during additive manufacturing of high strength β-titanium alloys, Addit. Manuf. 39 (2021), https://doi.org/10.1016/J.ADDMA.2021.101855 101855.
[47] C.H. Ng, M.J. Bermingham, D. Kent, M.S. Dargusch, High stability and high strength β-titanium alloys for additive manufacturing, Mater. Sci. Eng. A. 816 (2021), https://doi.org/10.1016/J.MSEA.2021.141326 141326.
[48] L.C. Zhang, D. Klemm, J. Eckert, Y.L. Hao, T.B. Sercombe, Manufacture by selective laser melting and mechanical behavior of a biomedical Ti-24Nb-4Zr-8Sn alloy, Scr. Mater. 65 (2011) 21–24, https://doi.org/10.1016/j.scriptamat.2011.03.024.
[49] R. Duan, S. Li, B. Cai, W. Zhu, F. Ren, M.M. Attallah, A high strength and low modulus metastable β Ti-12Mo-6Zr-2Fe alloy fabricated by laser powder bed fusion in-situ alloying, Addit. Manuf. 37 (2021), https://doi.org/10.1016/j.addma.2020.101708 101708.
[50] L. Zhou, T. Yuan, J. Tang, L. Li, F. Mei, R. Li, Texture evolution, phase transformation and mechanical properties of selective laser melted Ti-13Nb-13Zr, Mater. Charact. 145 (2018) 185–195, https://doi.org/10.1016/j.matchar.2018.08.053.
[51] L. Zhou, T. Yuan, R. Li, J. Tang, M. Wang, L. Li, C. Chen, Microstructure and mechanical performance tailoring of Ti-13Nb-13Zr alloy fabricated by selective laser melting after post heat treatment, J. Alloys Compd. 775 (2019) 1164–1176, https://doi.org/10.1016/j.jallcom.2018.10.030.
[52] J.J. Lewandowski, M. Seifi, Metal Additive Manufacturing: A Review of Mechanical Properties, Annu. Rev. Mater. Res. 46 (1) (2016) 151–186.
[53] W. Xu, M. Brandt, S. Sun, J. Elambasseril, Q. Liu, K. Latham, K. Xia, M. Qian, Additive manufacturing of strong and ductile Ti–6Al–4V by selective laser melting via in situ martensite decomposition, Acta Mater. 85 (2015) 74–84, https://doi.org/10.1016/J.ACTAMAT.2014.11.028.
[54] F. Schell, S. Alamri, A. Hariharan, A. Gebert, A.F. Lasagni, T. Kunze, Fabrication of four-level hierarchical topographies through the combination of LIPSS and direct laser interference pattering on near-beta titanium alloy, Mater. Lett. 306 (2022), https://doi.org/10.1016/J.MATLET.2021.130920 130920.
[55] N. Babacan, S. Pauly, T. Gustmann, Laser powder bed fusion of a superelastic Cu-Al-Mn shape memory alloy, Mater. Des. 203 (2021), https://doi.org/10.1016/J.MATDES.2021.109625 109625.
[56] T. Gustmann, A. Neves, U. Kühn, P. Gargarella, C.S. Kiminami, C. Bolfarini, J. Eckert, S. Pauly, Influence of processing parameters on the fabrication of a Cu-Al-Ni-Mn shape-memory alloy by selective laser melting, Addit. Manuf. 11 (2016) 23–31, https://doi.org/10.1016/J.ADDMA.2016.04.003.
[57] V.A.R. Henriques, E.T. Galvani, S.L.G. Petroni, M.S.M. Paula, T.G. Lemos, Production of Ti-13Nb-13Zr alloy for surgical implants by powder metallurgy, J. Mater. Sci. 45 (2010) 5844–5850, https://doi.org/10.1007/S10853-010-4660-8/TABLES/4.
[58] A.P. Hammersley, S.O. Svensson, M. Hanfland, A.N. Fitch, D. Hausermann, Two-dimensional detector software: From real detector to idealised image or two-theta scan, High Pressure Research 14 (4-6) (1996) 235–248.
[59] M. Fischer, D. Joguet, G. Robin, L. Peltier, P. Laheurte, In situ elaboration of a binary Ti–26Nb alloy by selective laser melting of elemental titanium and niobium mixed powders, Mater. Sci. Eng. C. 62 (2016) 852–859, https://doi.org/10.1016/J.MSEC.2016.02.033.
[60] M.J. Bermingham, S.D. McDonald, A.J. Buddery, D.H. Stjohn, M.S. Dargusch, Processing considerations for cast Ti–25Nb–3Mo–3Zr–2Sn biomedical alloys, Mater. Sci. Eng. C. 31 (2011) 1520–1525, https://doi.org/10.1016/J.MSEC.2011.06.011.
[61] D.Q. Martins, M.E.P. Souza, S.A. Souza, D.C. Andrade, C.M.A. Freire, R. Caram, Solute segregation and its influence on the microstructure and electrochemical behavior of Ti–Nb–Zr alloys, J. Alloys Compd. 478 (2009) 111–116, https://doi.org/10.1016/J.JALLCOM.2008.11.030.
[62] J. Haubrich, J. Gussone, P. Barriobero-Vila, P. Kürnsteiner, E.A. Jägle, D. Raabe, N. Schell, G. Requena, The role of lattice defects, element partitioning and intrinsic heat effects on the microstructure in selective laser melted Ti-6Al-4V, Acta Mater. 167 (2019) 136–148, https://doi.org/10.1016/J.ACTAMAT.2019.01.039.
[63] S. Banumathy, R.K. Mandal, A.K. Singh, Structure of orthorhombic martensitic phase in binary Ti–Nb alloys, J. Appl. Phys. 106 (9) (2009) 093518, https://doi.org/10.1063/1.3255966.
[64] D.L. Moffat, D.C. Larbalestier, The compctition between martensite and omega in quenched Ti-Nb alloys, Metall. Trans. A 19 (7) (1988) 1677–1686.
[65] A.R.G. Brown, D. Clark, J. Eastabrook, K.S. Jepson, The Titanium-Niobium System, Nat. 201 (4922) (1964) 914–915.
[66] J.A. Davidson, A.K. Mishra, P. Kovacs, R.A. Poggie, New surface-hardened, low-modulus, corrosion-resistant ti-13nb-13zr alloy for total hip arthroplasty, Biomed. Mater. Eng. 4 (1994) 231–243, https://doi.org/10.3233/BME-1994-4310.
[67] M. Bönisch, M. Calin, T. Waitz, A. Panigrahi, M. Zehetbauer, A. Gebert, W. Skrotzki, J. Eckert, Thermal stability and phase transformations of martensitic Ti–Nb alloys, Sci. Technol. Adv. Mater. 14 (5) (2013) 055004, https://doi.org/10.1088/1468-6996/14/5/055004.
[68] T. Vilaro, C. Colin, J.D. Bartout, L. Nazé, M. Sennour, Microstructural and mechanical approaches of the selective laser melting process applied to a nickel-base superalloy, Mater. Sci. Eng. A. 534 (2012) 446–451, https://doi.org/10.1016/j.msea.2011.11.092.
[69] Y. Zheng, R.E.A. Williams, S. Nag, R. Banerjee, H.L. Fraser, D. Banerjee, The effect of alloy composition on instabilities in the β phase of titanium alloys, Scr. Mater. 116 (2016) 49–52, https://doi.org/10.1016/J.SCRIPTAMAT.2016.01.024.
[70] S. Banerjee, P. Mukhopadhyay, Phase transformations: examples from titanium and zirconium alloys, Elsevier, 2010.
[71] L. Zhou, T. Yuan, R. Li, J. Tang, M. Wang, F. Mei, Microstructure and mechanical properties of selective laser melted biomaterial Ti-13Nb-13Zr compared to hot-forging, Mater. Sci. Eng. A. 725 (2018) 329–340, https://doi.org/10.1016/J.MSEA.2018.04.001.
[72] Y. Ohmori, T. Ogo, K. Nakai, S. Kobayashi, Effects of ω-phase precipitation on β→α, α″ transformations in a metastable β titanium alloy, Mater. Sci. Eng. A. 312 (2001) 182–188, https://doi.org/10.1016/S0921-5093(00)01891-8.
[73] P. Majumdar, S.B. Singh, M. Chakraborty, The role of heat treatment on microstructure and mechanical properties of Ti–13Zr–13Nb alloy for biomedical load bearing applications, J. Mech. Behav. Biomed. Mater. 4 (2011) 1132–1144, https://doi.org/10.1016/J.JMBBM.2011.03.023.
[74] M. Bönisch, Structural properties, deformation behavior and thermal stability of martensitic Ti-Nb alloys, 2016.
[75] M. Bönisch, M. Calin, J. Van Humbeeck, W. Skrotzki, J. Eckert, Factors influencing the elastic moduli, reversible strains and hysteresis loops in martensitic Ti-Nb alloys, Mater. Sci. Eng. C. 48 (2015) 511–520, https://doi.org/10.1016/j.msec.2014.12.048.
[76] X. Zhang, W. Wang, J. Sun, Y. Gao, S.J. Pennycook, Enhanced twinning-induced plasticity effect by novel {315}α″/{332}β correlated deformation twins in a Ti-Nb alloy, Int. J. Plast. 148 (2022), https://doi.org/10.1016/J.IJPLAS.2021.103132 103132.
[77] X. Ji, I. Gutierrez-Urrutia, S. Emura, T. Liu, T. Hara, X. Min, D. Ping, K. Tsuchiya, Twinning behavior of orthorhombic-α" martensite in a Ti-7.5Mo alloy, Sci. Technol. Adv. Mater. 20 (2019) 401–411, https://doi.org/10.1080/14686996.2019.1600201/FORMAT/EPUB.
[78] M. Bönisch, M. Calin, J. Van Humbeeck, W. Skrotzki, J. Eckert, Factors influencing the elastic moduli, reversible strains and hysteresis loops in martensitic Ti–Nb alloys, Mater. Sci. Eng. C. 48 (2015) 511–520, https://doi.org/10.1016/J.MSEC.2014.12.048.
[79] T. Ozaki, H. Matsumoto, S. Watanabe, S. Hanada, Beta Ti Alloys with Low Young's Modulus, Mater. Trans. 45 (2004) 2776–2779, https://doi.org/10.2320/MATERTRANS.45.2776.
[80] P. Castany, A. Ramarolahy, F. Prima, P. Laheurte, C. Curfs, T. Gloriant, In situ synchrotron X-ray diffraction study of the martensitic transformation in superelastic Ti-24Nb-0.5N and Ti-24Nb-0.5O alloys, Acta Mater. 88 (2015) 102–111, https://doi.org/10.1016/J.ACTAMAT.2015.01.014.
[81] E. Bertrand, P. Castany, Y. Yang, E. Menou, T. Gloriant, Deformation twinning in the full-α″ martensitic Ti–25Ta–20Nb shape memory alloy, Acta Mater. 105 (2016) 94–103, https://doi.org/10.1016/J.ACTAMAT.2015.12.001.
[82] P. Castany, Y. Yang, E. Bertrand, T. Gloriant, Reversion of a Parent 310 α″ Martensitic Twinning System at the Origin of 332 113 ©β Twins Observed in Metastable β Titanium Alloys, Phys. Rev. Lett. 117 (2016), https://doi.org/10.1103/PHYSREVLETT.117.245501/FIGURES/5/MEDIUM 245501.
[83] T. Ozaki, H. Matsumoto, S. Watanabe, S. Hanada, Beta Ti Alloys with Low Young's Modulus, (n.d.).
[84] Y. Mantani, M. Tajima, Effect of ageing on internal friction and elastic modulus of Ti–Nb alloys, Mater. Sci. Eng. A. 442 (2006) 409–413, https://doi.org/10.1016/J.MSEA.2006.03.124.
[85] Y. Mantani, M. Tajima, Phase transformation of quenched α″ martensite by aging in Ti–Nb alloys, Mater. Sci. Eng. A. 438–440 (2006) 315–319, https://doi.org/10.1016/J.MSEA.2006.02.180.
[86] S. Ozan, J. Lin, Y. Li, R. Ipek, C. Wen, Development of Ti-Nb-Zr alloys with high elastic admissible strain for temporary orthopedic devices, Acta Biomater. 20 (2015) 176–187, https://doi.org/10.1016/j.actbio.2015.03.023.

[87] M. Long, H.J. Rack, Titanium alloys in total joint replacement—a materials science perspective, Biomaterials. 19 (1998) 1621–1639, https://doi.org/10.1016/S0142-9612(97)00146-4.
[88] L.T. Duarte, S.R. Biaggio, R.C. Rocha-Filho, N. Bocchi, Surface characterization of oxides grown on the Ti–13Nb–13Zr alloy and their corrosion protection, Corros. Sci. 72 (2013) 35–40, https://doi.org/10.1016/J.CORSCI.2013.02.007.
[89] N.D. Tomashov, G.P. Chernova, Y.S. Ruscol, G.A. Ayuyan, The passivation of alloys on titanium bases, Electrochim. Acta. 19 (1974) 159–172, https://doi.org/10.1016/0013-4686(74)85012-7.
[90] J.M.A. El Kader, F.M.A. El Wahab, H.A. El Shayeb, M.G.A. Khedr, Oxide Film Thickening on Titanium in Aqueous Solutions in Relation to Anion Type and Concentration, Br. Corros. J. 16 (1982) 111–114, https://doi.org/10.1179/000705981798274977.
[91] A.G. Gad-Allah, H.A.A. El-Rahman, Kinetics of Open-Circuit Barrier Layer Formation on Metallic Surfaces in Aqueous Solutions, Corrosion. 43 (1987) 698–702, https://doi.org/10.5006/1.3583852.
[92] D.J. Blackwood, R. Greef, L.M. Peter, An ellipsometric study of the growth and open-circuit dissolution of the anodic oxide film on titanium, Electrochim. Acta. 34 (1989) 875–880, https://doi.org/10.1016/0013-4686(89)87123-3.
[93] T. Hurlen, S. Hornkjøl, Anodic growth of passive films on titanium, Electrochim. Acta. 36 (1991) 189–195, https://doi.org/10.1016/0013-4686(91)85200-Q.
[94] J. Vanhumbeeck, J.-F. Proost, Current Understanding of Ti Anodisation: Functional, Morphological, Chemical and Mechanical Aspects, Corros. Rev. 27 (2009) 117–204, https://doi.org/10.1515/CORRREV.2009.27.3.117.
[95] M.V. Diamanti, B. Del Curto, M. Pedeferri, Anodic Oxidation of Titanium: From Technical Aspects to Biomedical Applications, Https://Doi.Org/10.5301/JABB.2011.7429. 9 (2011) 55–69, https://doi.org/10.5301/JABB.2011.7429.
[96] F. El-Taib Heakal, K.A. Awad, Electrochemical Corrosion and Passivation Behavior of Titanium and Its Ti-6Al-4V Alloy in Low and Highly Concentrated HBr Solutions, Int. J. Electrochem. Sci. 6 (2011) 6483–6502.
[97] T.C. Niemeyer, C.R. Grandini, L.M.C. Pinto, A.C.D. Angelo, S.G. Schneider, Corrosion behavior of Ti–13Nb–13Zr alloy used as a biomaterial, J. Alloys Compd. 476 (2009) 172–175, https://doi.org/10.1016/J.JALLCOM.2008.09.026.
[98] M. Geetha, U.K. Mudali, N.D. Pandey, R. Asokamani, B. Raj, Microstructural and Corrosion Evaluation of Laser Surface Nitrided Ti-13Nb-13Zr Alloy, Surf. Eng. 20 (2013) 68–74, https://doi.org/10.1179/026708404225010595.
[99] J.M. Hernández-López, A. Conde, J. de Damborenea, M.A. Arenas, Correlation of the nanostructure of the anodic layers fabricated on Ti13Nb13Zr with the electrochemical impedance response, Corros. Sci. 94 (2015) 61–69, https://doi.org/10.1016/J.CORSCI.2015.01.041.
[100] S.Y. Yu, J.R. Scully, Corrosion and Passivity of Ti-13% Nb-13% Zr in Comparison to Other Biomedical Implant Alloys, Corros. 53 (1997) 965–976, https://doi.org/10.5006/1.3290281.
[101] M. Koike, K. Martinez, L. Guo, G. Chahine, R. Kovacevic, T. Okabe, Evaluation of titanium alloy fabricated using electron beam melting system for dental applications, J. Mater. Process. Technol. 211 (2011) 1400–1408, https://doi.org/10.1016/j.jmatprotec.2011.03.013.
[102] T. Balusamy, S. Kumar, T.S.N. Sankara Narayanan, Effect of surface nanocrystallization on the corrosion behaviour of AISI 409 stainless steel, Corros. Sci. 52 (2010) 3826–3834, https://doi.org/10.1016/j.corsci.2010.07.004.
[103] G.R. Argade, S.K. Panigrahi, R.S. Mishra, Effects of grain size on the corrosion resistance of wrought magnesium alloys containing neodymium, Corros. Sci. 58 (2012) 145–151, https://doi.org/10.1016/j.corsci.2012.01.021.